공학박사 학위논문

Efficient Small-Molecular-Weight Organic Solar Cells through Orientation Control and Nano-structuring

분자 배향과 나노구조 제어를 통한 고효율의 단분자 유기태양전지

2013 년 8 월

서울대학교 대학원
재료공학부
김 지 환

Efficient Small-Molecular-Weight Organic Solar Cells through Orientation Control and Nano-structuring

분자 배향과 나노구조 제어를 통한 고효율의 단분자 유기태양전지

지도 교수 김 장 주

이 논문을 공학박사 학위논문으로 제출함
2013 년 8 월

서울대학교 대학원
재료공학부
김 지 환

김지환의 박사 학위논문을 인준함
2013 년 8 월

위 원 장 _____ (인)

부 위 원 장 _____ (인)

위 원 _____ (인)

위 원 _____ (인)

위 원 _____ (인)

Abstract

Efficient Small-Molecular-Weight Organic Solar Cells through Orientation Control and Nano-structuring

Ji Whan Kim

Department of Materials Science and Engineering

The Graduate School of Engineering

Seoul National University

Due to the fast growing energy consumption and the growing environmental concerns over the climate change risks such as global warming, use of solar energy is one of the promising candidates for renewable sources of electricity. Among various solar cells, organic solar cells (OSCs) are considered to have large potential due to the fact that organic materials are cheap and easy to form a film with inexpensive process even in the large area. Unfortunately, OSCs have relatively low power conversion efficiency compared to other kinds of solar cells. Therefore the most important issue in OSCs is how to improve the power conversion efficiency (PCE).This thesis reports a couple of methods to improve the PCE of small molecular weight OSCs; nano-structuring and orientation control of active materials.

Small molecular weight OSCs have advantages of easy purification, good reproducibility, easy fabrication of multi-layered structure and so on over polymer based solar cells. One drawback of small molecular weight OSCs is located on the difficulties to form interpenetrating network between donor and acceptor molecules in nanometer scale because of the large entropy of mixing in the amorphous structure. A new method to form small-molecular based bulk heterojunction (BHJ) through alternating thermal deposition (ATD) is proposed, which is a simple modification of conventional thermal evaporation. The formation of a BHJ in copper(II) phthalocyanine (CuPc) and fullerene (C_{60}) systems is confirmed by atomic microscopy (AFM), grazing incidence X-ray small angle scattering (GISAXS), and absorption measurements. From the analysis of the data, CuPc|C_{60} films fabricated by ATD are composed of nanometer sized disk-shape CuPc nano grains and aggregated C_{60}, which explains the phase separation of CuPc|C_{60}. Compared with co-deposited OSCs, the ATD OSCs show significant enhanced performance. However ZnPc, which has the same crystalline structure with CuPc, did not show the improvement by ATD due to the initial growth difference. To understand the mechanism of ATD, the initial growth of CuPc on different substrate condition is monitored using GISAXS. Disk-type nano grains of CuPc were observed in an ultrathin CuPc layer evaporated on a hydrophilic Si

surface. The disk type grains consisted of a crystalline part and a non-crystalline part. The disk type grains were smaller in the case of CuPc on hydrophobic Si surface, which showed lower crystallinity with random distribution. Despite regularly distributed CuPc grains the mobility was lower in a thin film transistor device fabricated on a hydrophilic surface than on a hydrophobic surface due to the lower average density of the molecules relating to porous molecular packing between nanograins on a hydrophilic surface.

Improvement of the performance of OSCs was also achieved by controlling the molecular orientation. A highly efficient planar heterojunction OSC based on zinc phthalocyanine (ZnPc)/C_{60} is obtained by controlling the orientation of the ZnPc using copper iodide (CuI) as the interfacial layer. The proportion of face-on ZnPc molecules was increased significantly on the CuI layer compared to the layer without the CuI layer analyzed with wide angle X-ray scattering (WAXS) and optical absorption. The PCE of the orientation controlled planar heterojunction OSC was remarkably enhanced to 3.2% compared with 1.2% without the control of the molecular orientation. The mechanism of formation of the face-on molecular orientation of ZnPc on CuI layer is proposed. Using the two different incidence angles in the glazing incidence wide angle x-ray scattering (GIWAXS), it turns out that the ZnPc layer on the (111) γ phase

CuI is the β phase ZnPc with ($\bar{1}$01) orientation which is transformed to (313) gamma phase ZnPc as the film growth. These phase transitions can be explained with quasi epitaxial growth.

Keywords: organic solar cells, bulk heterojunction, molecular orientation, crystalline structure

Student Number: 2007-30178

Contents

Abstract.....i

Contents v

List of Tables ix

List of Figures.....x

CHAPTER 1. INTRODUCTION..... 1

1.1 Introduction to organic solar cells.....1

1.2 Operation principles of organic solar cells 5

1.3 Outline of the thesis 12

1.4 Bibliography 15

CHAPTER 2. NANO-STRUCTURE CONTROL WITH ALTERNATING THERMAL DEPOSITION..... 17

2.1 Introduction.....17

2.2 Experiments.....19

2.3 Results and Discussion.....21

2.3.1 CuPc and C_{60} system.....25

2.3.2 ZnPc and C_{60} system.....41

2.4 Conclusion 55

2.5 Bibliography.....56

CHAPTER 3. INITIAL GROWTH OF PLANAR ORGANIC MOLECULES AFFECTED BY SUBSTRATE SURFACE ENERGY 59

3.1 Introduction.....59

3.2 Experiments.....62

3.3 Results and discussion 64

3.4 Conclusion 79

3.5 Bibliography.....80

CHAPTER 4. HIGH PERFORMANCE ORGANIC PLANAR HETERO-JUNCTION SOLAR CELLS BY CONTROLLING THE MOLECULAR ORIENTATION 82

4.1 Introduction **82**

4.2 Experiments **85**

4.3 Results and discussion **87**

4.3.1 ZnPc planar heterojunction OSCs 87

4.3.2 Introducing CuI to ATD bulk heterojunction OSCs 100

4.4 Conclusion **104**

4.5 Bibliography **105**

CHAPTER 5.THE CRYSTALLINE STRUCTURE OF THE INTERFACE BETWEEN ORIENTATION CONTROLLED ZINC PHTHALOCYANINE AND COPPER IODIDE **107**

5.1 Introduction **107**

5.2 Experiments **109**

5.3 Results and discussions **110**

5.4 Conclusion **119**

5.5 Bibliography **120**

국문초록.....122

CURRICULUM VITAE.....125

List of Tables

Table 2.1 Parameters obtained from x-ray reflectivity curve analysis.....29

Table 2.2 The power-conversion efficiency, PCE, short-circuit current, J_{SC}, open circuit voltage, V_{OC} and fill factor, *FF* of planar heterojunction (ITO/CuPc 20 nm/C_{60} 40 nm/BCP 8 nm/Al), PHJ, co-deposited (ITO/CuPc 3 nm/CuPc:C_{60} 1:1 40 nm/C_{60} 10 nm/BCP 8 nm/Al), and ATD (ITO/CuPc 3 nm/ATD CuPc|C_{60} 1:1 40 nm/C_{60} 10 nm/BCP 8 nm/Al) 40

Table 4.1 The power-conversion efficiency, PCE, short-circuit current, J_{SC}, open circuit voltage, V_{OC} and fill factor, *FF* of codeposited and ATD OSCs with or without CuI layer 102

List of Figures

Figure 1.1 Examples of application of OSCs. (top) [1] Oxford Photovoltaics uses non-toxic organic solar cell materials printed directly on to glass to produce clean energy. (bottom) Flexible OSC module by Fraunhofer ISE. [2] 2

Figure 1.2 Best research-cell efficiencies for various solar cells by the time. [7].....4

Figure 1.3 The operation mechanism of planar heterojunction organic solar cells. The excitons formed in shaded region contribute to current. 6

Figure 1.4 Conceptual drawing of bulk heterojunction organic solar cell. The exactions generated in the shaded region can be dissociated. 8

Figure 1.5 J-V characteristics for typical solar cells under illumination. Arrows indicates the ways to improve the solar cell performances....9

Figure 1.6 Importance of molecular orientation on the performance of organic solar cells 11

Figure 2.1a A schematic diagram of alternating thermal deposition (ATD) and molecular structures of CuPc and C_{60}. 23

Figure 2.1b Proposed bulk heterojunction formation mechanism with ATD 24

Figure 2.2(a) X-ray reflectivity measurement about CuPc 50nm (blue), ATD CuPc|C_{60} (red), and co-deposited CuPc:C_{60} (black). (b), (c), (d) GISAXS images about CuPc 50nm, ATD CuPc|C_{60}, co-deposited CuPc:C_{60}, respectively. 26

Figure 2.3(a), (b), (c) horizontal direction cuts of the 2D images and model fit result about CuPc 50nm, ATD CuPc|C_{60}, co-deposited CuPc:C_{60} (red open circles: 0.1° incident angle data, blue closed circles: 0.25° incident angle data, lines: fitting result). Data of CuPc 50nm and ATD were fitted using a disc model. In the case of co-deposited CuPc:C_{60}, it was fitted using both a disk and a sphere model as shown in the inset of (c) (black dotted line: disk model, red solid line: sphere model). The positions of the line cutting are marked as dotted lines in the images of Fig. 2.2 (b), (c) and (d). Inset: 250×250 nm^2 AFM images of (a) CuPc, (b) ATD CuPc|C_{60} and (c) co-deposited CuPc:C_{60}. 27

Figure 2.4 Measured UV-spectra of co-deposited (black) and ATD (red) films are compared to calculation (black) assuming a homogeneous mixture ($0.5\alpha_{CuPc} + 0.5\alpha_{C60}$) with no interaction. Arrows indicate the wavelength of CuPc and C_{60} aggregation absorptions.....36

Figure 2.5 J-V characteristics of PHJ (blue triangles) and BHJ OSC devices fabricated by ATD (red circles) and co-deposition (black

squares) methods under AM 1.5 illumination. In the OSC device with ATD, J_{SC}, V_{OC}, *FF*, and PCE were 8.34 mA cm^{-2}, 0.41 V, 0.45, and 1.56%, respectively. Inset: J-V characteristics of the same figure with longer range. 39

Figure 2.6 J-V characteristics of ZnPc-C_{60} PHJ (red circles) and BHJ OSCs fabricated by ATD (green triangles) and co-deposition (blue triangles) methods under AM 1.5 illumination.....43

Figure 2.7 (a)(b) GIWAXS 2D images of the ZnPc and CuPc for 5 nm and 50 nm thick films, respectively; (c) The normalized lattice parameters, (d) crystal domain size, and (f) angular dispersion of γ-phase ZnPc as a function of the film thickness. The angular dispersion indicates the FWHM of the γ(200) peak in the circular direction, as shown in the dotted line in the inset (e). The peak positions of the (200), (002), and (010) orientation of the γ-phase are shown in the GIWAXS 2D diffraction images. 46

Figure 2.8 GISAXS images of ZnPc and CuPc for 5 nm. 49

Figure 2.9 Binding energy vs intermolecular distance with two different configurations for ZnPc and CuPc. 52

Figure 2.10 Binding energy vs intermolecular distance calculation result for CuPc-CuPc, ZnPc-ZnPc, CuPc-C_{60}, and ZnPc-C_{60}.....53

Figure 3.1 Transfer characteristics of CuPc OFET on a hydrophilic substrate (red line) and on hydrophobic substrate (blue line).....65

Figure 3.2 AFM images of (a) CuPc on a hydrophobic (ODTS treated) surface and (b) hydrophilic (Piranha treated) on surface. The R_{rms} roughness of ODTS treated surface is 0.51 nm, while R_{rms} of the Piranha treated surface is 0.25 nm, respectively. (scale bar: 200nm) 66

Figure 3.3 (a) and (b) are measured GIWAXS and GISAXS images of a CuPc layer (5 nm) on a hydrophilic Si surface, respectively. (c) is a GISAXS simulation image using a disc type structure factor. The central rod originated from the specular scattering is not calculated in SAXS simulation. The two wings of SAXS pattern are originated from the interference between nano discs. (d) and (e) are GIWAXS and GISAXS images of a CuPc layer (5 nm) on an ODTS treated hydrophobic Si surface, respectively. (f) is a GISAXS simulation image of CuPc layer on an ODTS treated hydrophobic Si surface. Comparing to (c), the central rod is shown due to large disordering of the interference between nano dics. 67

Figure 3.4 The x-ray reflectivity measurement for CuPc film on a hydrophilic surface (red open circle) and on a ODTS (hydrophobic) surface (blue closed circle). Solid lines indicates fitting. 73

Figure 3.5 Model of CuPc ultra-thin layers on a hydrophilic surface and on a hydrophobic surface 74

Figure 3.6 Temperature dependence of mobilities of OFET devices fabricated on a hydrophilic surface and a hydrophobic surface. 77

Figure 4.1 The current density-voltage characteristics of ITO/ZnPc 25 nm/C_{60} 40 nm/BCP 8 nm/Al 100 nm (black squares) and ITO/CuI 3 nm/ZnPc 25 nm/C_{60} 40 nm/BCP 8 nm/Al 100 nm (red circles) under dark (open symbols) and under AM1.5 solar simulator illumination (closed symbols). 88

Figure 4.2(a) UV-VIS absorption spectra of CuI 3 nm, ZnPc 20 nm, and CuI 3 nm/ZnPc 20 nm on quartz substrates. 2 guide lines at 628 nm and 704 nm are drawn at the absorption peaks of ZnPc 20 nm. (b) IPCE spectra of ITO/ZnPc 25 nm/C_{60} 40 nm/BCP 8 nm/Al (black squares) and ITO/CuI 3 nm/ZnPc 25 nm/C_{60} 40 nm/BCP 8 nm/Al (red circles). 89

Figure 4.3 (a) and (b) are GIWAXS images of ZnPc on Si and CuI surfaces, respectively. (c) and (d) are vertical and horizontal line cut data of GIWAXS images as marked by dotted lines in (a) and (b). As shown in (c), the (010) peak relating to the lying configuration was observed in the vertical line cut data on the CuI surface. The (303) peak of the horizontal line cut data also supports the lying

configuration of ZnPc molecules on the CuI surface. Dotted lines in (c) indicate peak fittings or (010) and (007). 91

Figure 4.4 UPS spectra of ITO/ZnPc 94

Figure 4.5 UPS spectra of ITO/ZnPc/C_{60}.....95

Figure 4.6 UPS spectra of ITO/CuI/ZnPc 96

Figure 4.7 UPS spectra of ITO/CuI/ZnPc/C_{60} 97

Figure 4.8 Energy band diagram of ITO/ZnPc/C_{60} and ITO/CuI/ZnPc/C_{60} extracted from the UPS measurement. (All numbers are in eV units) 98

Figure 4.9 The current density-voltage characteristics of 4 devices: without CuI layer/codep. (black circles), without CuI layer/ATD (red squares), with CuI layer/codep. (blue triangles), and with CuI layer/ATD (green triangles) under dark (closed symbols) and under AM1.5 solar simulator illumination (open symbols).....101

Figure 5.1 The unit cell parameters of β phase and γ phase ZnPc used to index the peaks.....111

Figure 5.2 GIWAXS images of two different incidence angles; 0.05° and 0.20°. 0.20° data shows the bulk property of the film and 0.05° data shows the property of the surface of the film (ZnPc 20 nm/CuI 3 nm/Si) due to the penetration depth difference with the incident angle. In the bulk film, ZnPc beta phase appears, which is not observed in

the surface of the film, indicating that beta phase exist close to CuI layer.....113

Figure 5.3 XRD of Si/CuI (3 nm)/ZnPc (20 nm) at the high q region...114

Figure 5.4 Line cut of GIWAXS image shown in Figure 5.2 in Q_z direction for incidence angle of 0.05 (black squares) and 0.20 (blue triangles). Blue lines indicate peak fitting with Gaussian functions based on their crystal structures.....117

Figure 5.5 Proposed layer structure and its mechanism. When ZnPc layer is thermally deposited on CuI layer, thin beta phase ZnPc with (101) direction forms on the (111) CuI layer. Then (313) gamma ZnPc sits on the beta ZnPc layer. Quasi organic epitaxial growth showing the super lattice as drawn above. 118

Chapter 1. Introduction

1.1 Introduction to organic solar cells

A solar cell, so called a photovoltaic cell, is an electrical device that converts the energy of light into electricity by the photovoltaic effect. Due to the fast growing energy consumption and the growing environmental concerns over the climate change risks such as global warming, using solar energy is one of the promising candidates for renewable sources of electricity. Using solar energy reduces the dependence on fossil fuels and is environmentally clean compared to other forms of electricity production. Current photovoltaic cells in the markets are mostly based on silicon or inorganic semiconductors like GaAs or CdTe. However, the fabrication costs, the rarity of the materials and the use of toxic solvents in the fabrication process are the problems to be solved. Many of these problems can be solved using organic materials.

Organic materials are cheap and easy to form a film with inexpensive process even in the large area cells. Organic solar cells (OSCs) require a few hundred nanometer thick film, they can be light and flexible, therefore have great possibility for mobile applications. Figure 1.1 shows some examples of applications for OSCs, transparent and flexible solar cells using organic materials.

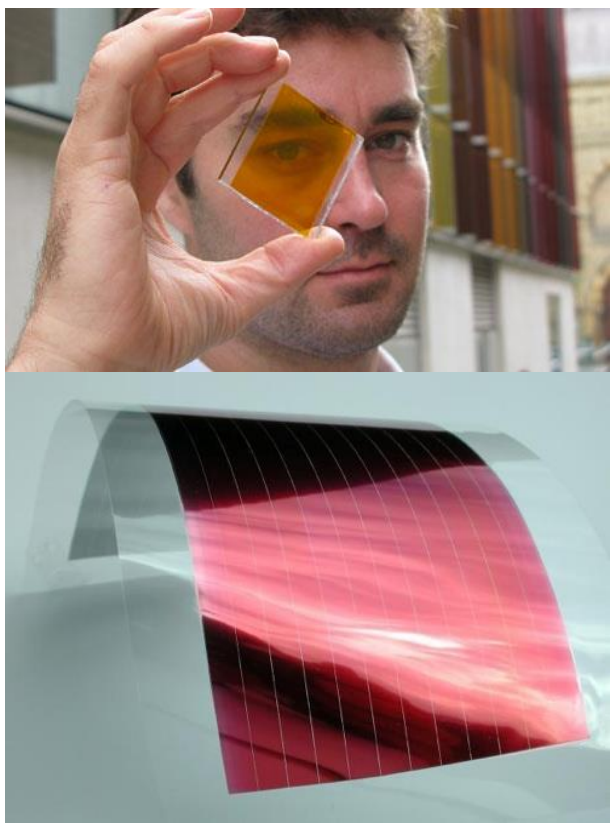

Figure 1.1 Examples of application of OSCs. (top)[1]Oxford Photovoltaics uses non-toxic organic solar cell materials printed directly on to glass to produce clean energy. (bottom) Flexible OSC module by Fraunhofer ISE.[2]

Although OSCs has the attractive features such as the use of roll-to-roll processes generating cheap, flexible and large-area devices, the power conversion efficiency (PCE) is still low compared to the inorganic solar cells. Figure 1.2 shows the current status of photovoltaic devices. The highest efficiency reported is 44.4% with multiple-junction concentrated photovoltaics using InGaP, GaAs, and InGaAs [3], however the PCEs of OSCs are around 10%[4]. Many research efforts improved the efficiency and helped to understand the basic processes and barriers, the PCEs have improved rapidly[5][6].

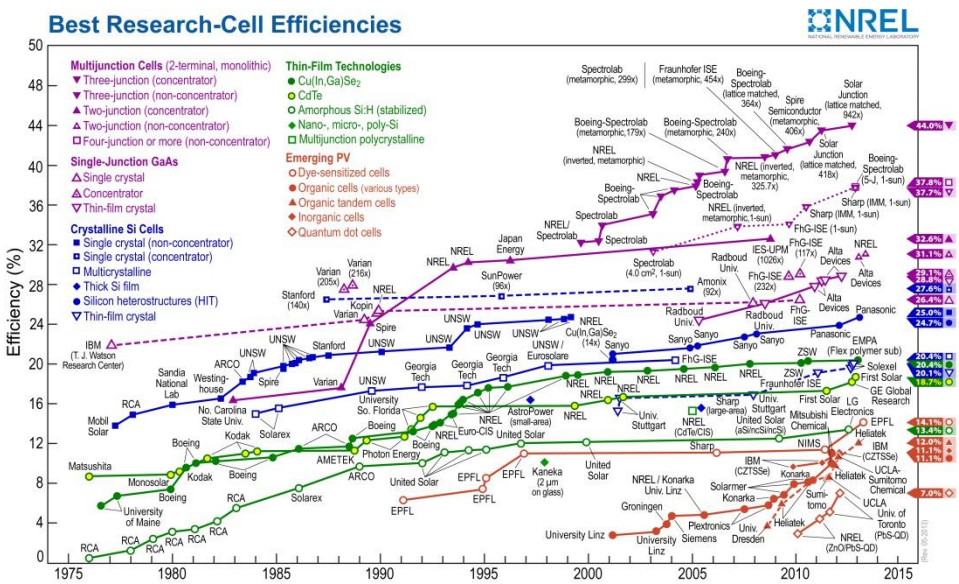

Figure1.2 Best research-cell efficiencies for various solar cells by the time. [7]

1.2 Operation principles of organic solar cells

The operation mechanism of typical planar (or bi-layer) heterojunction OSCs[8] is shown in Figure 1.3. The planar heterojunction OSCs contains electron donor and electron acceptor in between the conductive electrodes. These two layers have differences in electron affinity and ionization energy, therefore local electric fields exists. Once the organic materials absorb the light, the excitons are formed. These excitons diffuse to donor-acceptor interface then dissociate to holes and electrons due to the electric fields at the interface. Then the holes and electrons are collected to the conductive electrodes. The problem in these planar heterojunction OSCs lies in the exciton diffusion length of the organic materials. The diffusion length of organic materials is typically on the order of 10 nm. In order to generate the hole and electron, the excitons have to diffuse to the donor-acceptor interface. The organic materials need at least 100 nm to absorb most of the light. This indicates that a small fraction of excitons reach to the interface contributing to electricity generation. Only the excitons that formed in the shaded region in Figure 1.3 are able to generate current.

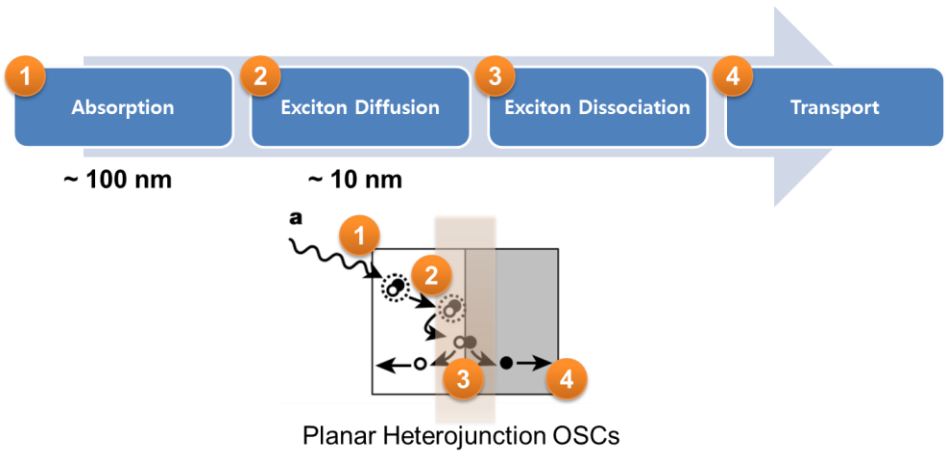

Figure 1.3 The operation mechanism of planar heterojunction organic solar cells. The excitons formed in shaded region contribute to current.

To overcome the tradeoff between the absorption length and the exciton diffusion length in the planar heterojunction OSCs, mixed donor-acceptor layers were adopted to create an interpenetrating network by phase separation on a nanoscale. Figure 1.4 shows a typical conceptual drawing of bulk heterojunction OSCs. If the length scale of the mixture is similar to the exciton diffusion length, most of the exciton generated by absorbing light can reach to the interface, where exciton dissociation occurs. The shaded region in the figure contributes to current.

A typical current-voltage characteristic under illumination is shown in Figure 1.5. The point where the current is zero is open circuit voltage, V_{OC}. J_{SC} represents short circuit current where the OSC is under short circuit condition, zero applied bias. The maximum point of power generated, P_{max}, for the device can be obtained from the J-V curve. The ration between P_{max} and the product of J_{SC} and V_{OC} is called fill factor (FF). To characterize the performance of solar cells, power conversion efficiency (PCE) is mostly used. The PCE is defined as Equation 1-1.

$$PCE = \frac{P_{max}}{P_{light}} = \frac{V_{oc} \cdot J_{sc} \cdot FF}{P_{light}} \qquad (1-1)$$

where P_{light} represent incident light power

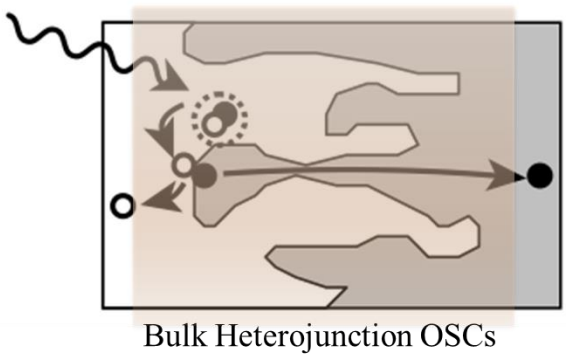

Figure 1.4 Conceptual drawing of bulk heterojunction organic solar cell.

The exactions generated in the shaded region can be dissociated.

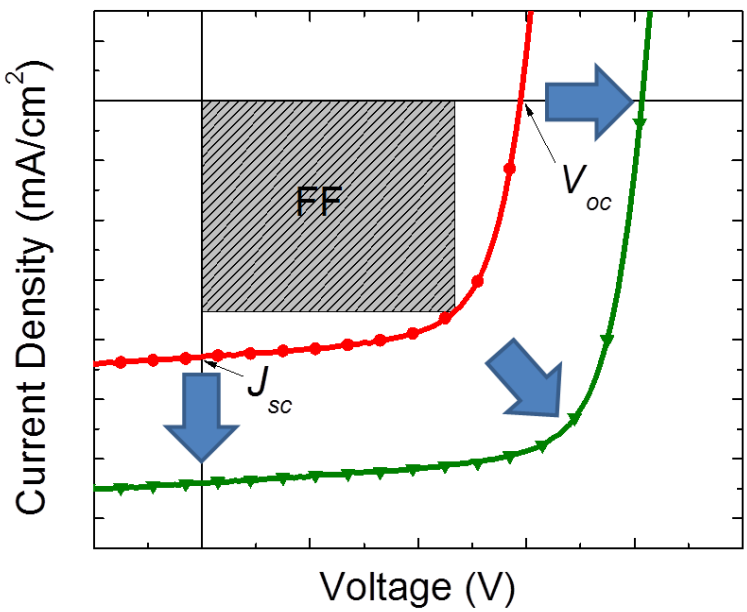

Figure 1.5 J-V characteristics for typical solar cells under illumination. Arrows indicates the ways to improve the solar cell performances.

To enhance the performances of OSCs, J_{SC}, V_{OC}, and *FF* need to be enhanced. J_{SC} is related with the amount of absorbed light within the range of exciton diffusion length[9]. V_{OC} is closely related to the energy difference between the highest occupied molecular orbital (HOMO) of the donor and the lowest unoccupied molecular orbital (LUMO)[10,11]. FF is more complicated, however it is known to be related with the charge transport properties of donor and acceptor materials.

To obtain higher J_{SC}, bulk heterojunction with efficient interpenetrating network is one of the solutions. Another solution to enhance the J_{SC} is controlling the molecular orientation. By matching the molecular transition dipole moment to the electric field of incident light, the total amount of absorption within the exciton diffusion length can be enhanced. In addition well-ordered molecular orientation affects not only HOMO-LUMO energy levels but also the ionization potentials in organic thin films[12-14] resulting change in V_{OC}. High electron and hole mobilities are required to achieve a high *FF* favoring the face-on packing of molecules along with high crystallinity[15]. Figure 1.6 summarizes the effects of molecular orientation to the OSC performances.

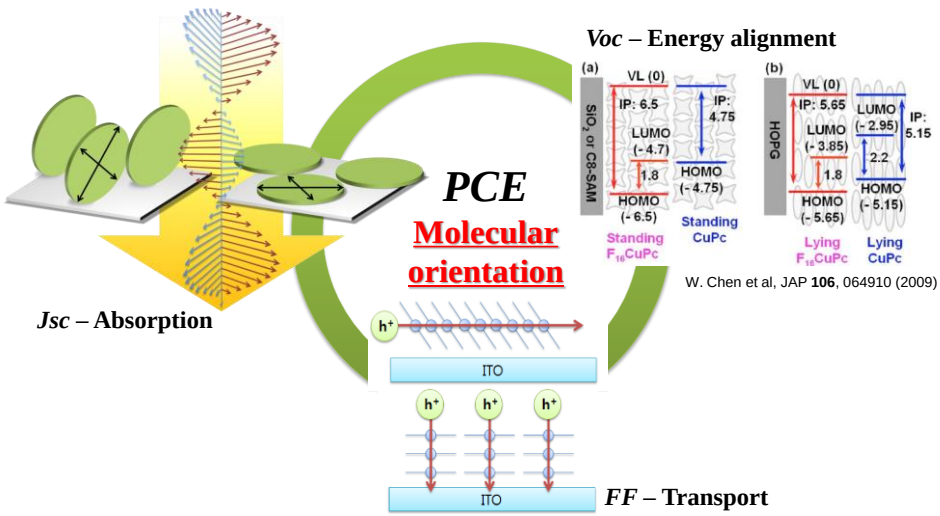

Figure 1.6 Importance of molecular orientation on the performance of organic solar cells

1.3 Outline of the thesis

In Chapter 2, a new method to form small-molecular-weight based bulk heterojunction (BHJ) through alternative (or alternating) thermal deposition (ATD) is proposed, which is a simple modification of conventional thermal evaporation. By ATD, the thickness of alternating donor and acceptor layers was precisely controlled down to 0.1 nm, which is critical to form BHJs. The formation of a BHJ in copper(II) phthalocyanine (CuPc) and fullerene (C_{60}) systems is confirmed by atomic force microscopy (AFM), grazing incidence X-ray small angle scattering (GISAXS), and absorption measurements. From the analysis of the data, CuPc|C_{60} films fabricated by ATD are composed of nanometer sized disk-shape CuPc nano grains and aggregated C_{60}, which explains the phase separation of CuPc|C_{60}. Compared with tradition co-deposited film, the OSCs show significantly enhanced performance.

In Chapter 3, the initial growth of CuPc on different substrate condition is monitored using GISAXS. Disk-type nano grains of CuPc were observed in an ultrathin CuPc layer evaporated on a hydrophilic Si surface. The disk type grains consisted of a crystalline part and a non-crystalline part. The disk type grains were smaller in the case of CuPc on hydrophobic Si surface, which showed lower crystallinity with random distribution. Despite regularly distributed CuPc grains the mobility was lower in a thin

film transistor device fabricated on a hydrophilic surface than on a hydrophobic surface due to the lower average density of the molecules relating to porous molecular packing between nanograins on a hydrophilic surface.

In Chapter 4, the effects of molecular orientation control to the performance of OSCs are mentioned. A highly efficient planar heterojunction OSC based on zinc phthalocyanine (ZnPc)/C_{60} by controlling the orientation of the ZnPc by using copper iodide (CuI) as the interfacial layer is obtained. The proportion of face-on ZnPc molecules was increased significantly on the CuI layer compared to the layer without the CuI layer analyzed with wide angle X-ray scattering (WAXS) and optical absorption. The PCE of the orientation controlled planar heterojunction OSC was remarkably enhanced to 3.2% compared with 1.2% without the control of the molecular orientation.

In Chapter 5, a mechanism of formation of the face-on molecular orientation of ZnPc on CuI layer is proposed. Using the two different incidence angles in the glazing incidence wide angle x-ray scattering (GIWAXS), the crystalline structures of ZnPc at the surface and that of ZnPc at the CuI interface were distinguishable. β phase ZnPc with $(\bar{1}01)$ orientation were formed on the (111) γ phase CuI and (313) γ phase ZnPc

on $(\bar{1}01)$$\beta$-phase ZnPc. These phase transitions can be explained with quasi epitaxial growth.

1.4 Bibliography

[1] "Colourful 'solar glass' means entire buildings can generate clean power | Environment | guardian.co.uk," can be found under http://www.guardian.co.uk/environment/2013/feb/12/printed-solar-glass-panels-oxford-photovoltaics

[2] "Organic Solar Cells: Electricity From A Thin Film," can be found under http://www.sciencedaily.com/releases/2008/02/080206154631.htm**.**

[3] "Sharp Develops Concentrator Solar Cell with World's Highest Conversion Efficiency of 44.4% | Press Releases | Sharp Global," can be found under http://sharp-world.com/corporate/news/130614.html

[4] J. You, C.-C. Chen, Z. Hong, K. Yoshimura, K. Ohya, R. Xu, S. Ye, J. Gao, G. Li, Y. Yang, *Advanced Materials***2013**, online published, DOI: 10.1002/adma.201300964.

[5] P. Heremans, D. Cheyns, B. P. Rand, *Account of Chemical Research* **2009**, *42*, 1740–1747.

[6] J.-L. B. Das, J. E. Norton, J. Cornil, V. Coropceanu, *Account of Chemical Research***2009**, *42*, 1691–1699.

[7] "NREL: National Center for Photovoltaics Home Page," can be found under http://www.nrel.gov/ncpv/

[8] C. W. Tang, *Appl. Phys. Lett.***1986**, *48*, 183–185.

[9] J. Lee, S.-Y. Kim, C. Kim, J.-J. Kim, *Appl. Phys. Lett.***2010**, *97*,

083306.

[10] K. Vandewal, K. Tvingstedt, A. Gadisa, O. Inganäs, J. V. Manca, *Nature Materials***2009**, *8*, 904–909.

[11] B. Qi, J. Wang, *J. Mater. Chem. VL - IS* -**2012**, *22*, 24315–24325.

[12] S. Fabiano, H. Yoshida, Z. Chen, A. Facchetti, M. A. Loi, *ACS Applied Materials and Interfaces***2013**, 130501114221008.

[13] S. Duhm, G. Heimel, I. Salzmann, H. Glowatzki, R. L. Johnson, A. Vollmer, J. P. Rabe, N. Koch, *Nature Materials***2008**, *7*, 326–332.

[14] W. Chen, S. Chen, S. Chen, Y. L. Huang, H. Huang, D.-C. Qi, X. Y. Gao, J. Ma, A. T. S. Wee, *Journal of Applied Physics***2009**, *106*, 064910.

[15] R. R. Lunt, J. B. Benziger, S. R. Forrest, *Advanced Materials***2010**, *22*, 1233–1236.

Chapter 2. Nano-structure control with alternating thermal deposition

2.1 Introduction

The performances of organic solar cells (OSCs) have improved significantly in recent years[1-5]. To overcome the tradeoff between the absorption length (L_a, ~100 nm) and the exciton diffusion length (L_D, ~10 nm) in donor/acceptor (DA) planar heterojunction (PHJ) OSCs [6],mixed DA layers were adopted to create an interpenetrating network by phase separation on a nanoscale[2-5],[7].This bulk heterojunction (BHJ) concept has achieved large success in polymer based solar cells[3,4]. In small molecular OSCs, however, co-deposited mixed layers have not been so successful as in polymer solar cells due to a large entropy of mixing to reduce the tendency of the phase separation and the formation of interpenetrating networks. Nevertheless, co-deposited layers have been believed to form BHJs, which does not seem to be true because of the lack of any crystalline phase in the x-ray diffraction of the co-deposited layers[8]. Although the device performance was improved by co-deposition of donor and acceptor materials, the direct evidence of the mixed layer has not been reported yet. Despite the successful fabrication of BHJs with organic vapor phase deposition[9,10], co-deposition by

thermal evaporation is still widely used to form the mixed layer of donor and acceptor materials in many groups because of the simplicity of the technique and the accessibility of the equipment.

New simple and easy controlled growth of small-molecular-weight OSCs with modified thermal evaporation, i.e. alternative (or alternating) thermal deposition (ATD) is proposed. With ATD, we succeeded to control the thicknesses of donor and acceptor layers separately down to 0.1 nm. OSCs fabricated using the ATD method showed significantly enhanced power conversion efficiency compared to co-deposited OSCs. We compared the difference in the morphology of the co-deposited layers and ATD layers using grazing incidence x-ray small angle scattering (GISAXS). This is the first report about nano structural distribution of donor and acceptor molecules in a co-deposited layer and ATD layer.

2.2 Experiments

X-ray reflectivity (XRR) and GISAXS (grazing incidence small angle x-ray scattering) measurements were done at the 5A beam line of Pohang Light Source of Koreafor copper(II) phthalocyanine (CuPc) based samples. The x-ray energy was 11.6 keV. GISAXS was done at two different incident angles of 0.1° (lower than the critical angle of CuPc:C_{60}) and 0.25° (higher than the critical angle of CuPc:C_{60}) to distinguish x-ray signals from the surface region and the bulk region. The distance from the sample to detector was 2 m, and a 2D image plate was used for the GISAXS measurements. For zinc phthalocyanine (ZnPc) based samples, x-ray measurements were performed at the 12ID-B and 12ID-C beam lines of the Advanced Photon Source (APS) at the Argonne National Laboratory. The x-ray energy was 12 eV. The distance from the sample to the detector was 1994.6 mm for GISAXS. A PILATUS 2M detector was used.

Atomic force microscope (AFM) topographic and phase images were taken in a PSIA XE-100 scanning probe microscope with non-contact mode. CuPc, co-deposited CuPc:C_{60} and ATD CuPc|C_{60} films are deposited under vacuum of 10^{-7} torr on Si wafer cleaned with piranha solution.

The UV-VIS absorption spectra of studied films were recorded with a VARIAN Cary 5000 UV-Vis spectrophotometer. 50 nm-thick films were thermally evaporated on clean quartz substrates.

The ITO-coated glass substrates were cleaned with acetone and isopropyl alcohol. The substrates were exposed to UV–O_3 for 10 min before use. CuPc, ZnPc, C_{60}, 2,9-dimethyl-4,7-dipheyl-1,10-phenanthroline (BCP) and Al are thermally deposited under vacuum of 10^{-7} torr. All layers are successively evaporated without breaking the vacuum and all devices were encapsulated in N_2 ambient before photocurrent measurements. The photocurrents were measured under illumination from an AM1.5 solar simulator (300W Oriel 91160A). The light intensity was carefully calibrated using a standard silicon solar cell (NREL). A Keithley 237 source measurement unit was used for current density–voltage characteristics

2.3 Results and Discussion

Figure 2.1a shows the schematic diagram of the ATD method. A vacuum chamber is separated into two compartments with a shield. A donor (D) material and an acceptor (A) material are evaporated in different compartments simultaneously under vacuum. The deposition rates of the molecules are separately controlled. The substrates are located off center of the rotating axis so that donor and accepter molecules can be deposited alternatively by rotation. This is a very simple method to deposit alternative DA layers in series. Moreover the thickness of the alternatively deposited layers can be controlled easily down to sub-monolayer by controlling the rotation speed and deposition rates, which is a critical factor to grow BHJs in the alternatively deposited films. When the thickness of each layer per rotation is thinner than a few angstroms (less than the thickness of the monolayer), discontinuous films are formed regardless of the film forming mechanisms[11]. Once a discontinuous film of one component is formed, successive deposition of other component is likely to fill the gap by aggregation to create nano-crystalline BHJs if the interaction energy between the D-A molecules is smaller than the interaction energy between the same molecules. This technique allows easy control of the thermodynamic parameters such as the composition and the growing temperature as well as the kinetic

parameters such as the deposition rate. Figure 2.1b shows the proposed mechanism of forming efficient bulk heterojunction using ATD.

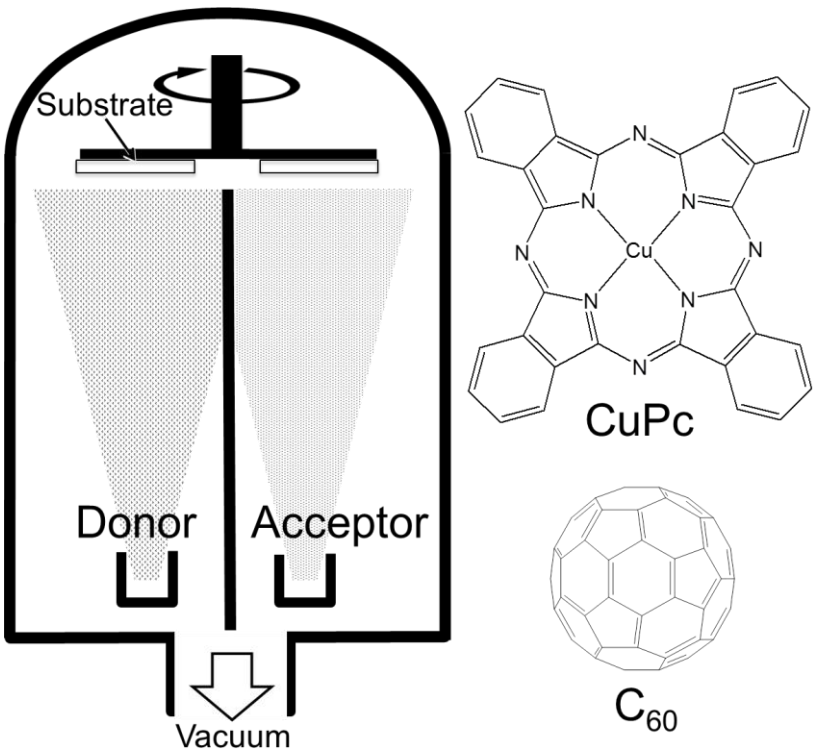

Figure 2.1aA schematic diagram of alternating thermal deposition (ATD) and molecular structures of CuPc and C_{60}.

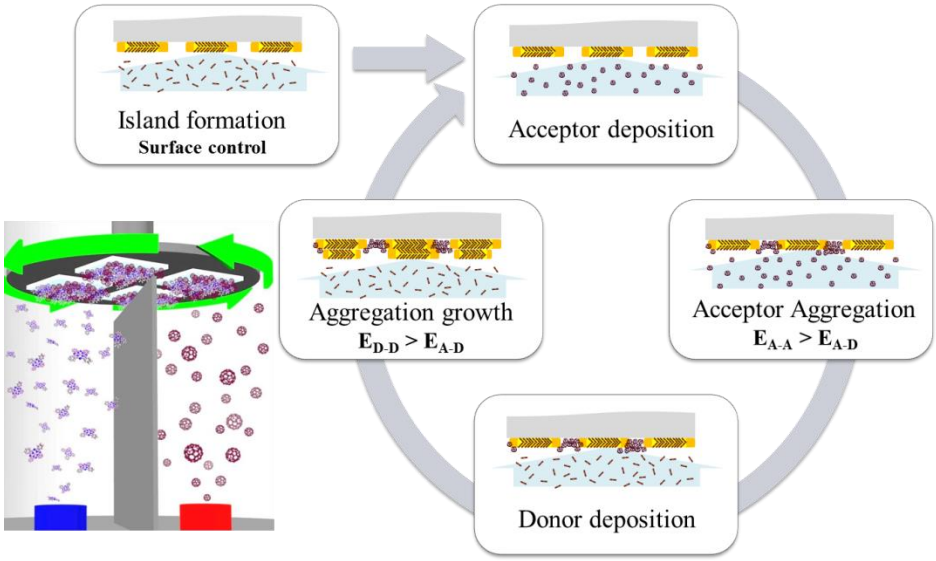

Figure 2.1b Proposed bulk heterojunction formation mechanism with ATD

2.3.1 CuPc and C_{60} system

In this study, we used copper (II) phthalocyanine (CuPc) and fullerene (C_{60}) as donor and acceptor molecules to demonstrate the concept of ATD. The CuPc|C_{60} is expected to form BHJs by the ATD method because the interaction energy between CuPc and C_{60} (0.044 eV) is much lower than that between the same molecules (CuPc: 0.867 eV, C_{60}: 1.5 eV)[10]. For the demonstration, a 1.09-nm-thick layer of CuPc|C_{60} (0.545 nm|0.545 nm) is formed in each rotation of the substrate. The deposition rate of each source was maintained to 1 Å s^{-1}.

The structure of CuPc|C_{60} film formed by ATD was analyzed with x-ray reflectivity and GISAXS measurement. Figure 2.2a shows the reflectivity curves of 50 nm thick layers of CuPc (blue dots), ATD CuPc|C_{60} (red dots) and co-deposited CuPc:C_{60} (black dots) on Si substrates, respectively. The structural information of the films was obtained by the analysis of the data using a single layer model on a silicon substrate with a kinematic approximation about the x-ray reflection in a thin film system[12,13].

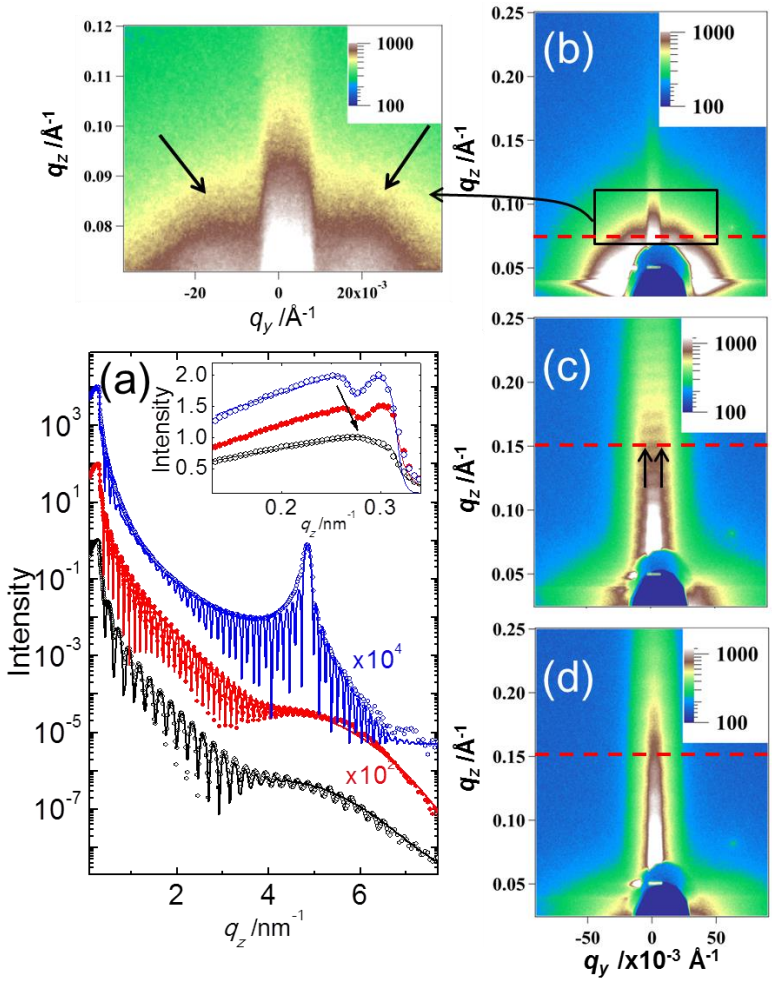

Figure 2.2(a) X-ray reflectivity measurement about CuPc 50nm (blue), ATD CuPc|C_{60} (red), and co-deposited CuPc:C_{60} (black). (b), (c), (d) GISAXS images about CuPc 50nm, ATD CuPc|C_{60}, co-deposited CuPc:C_{60}, respectively.

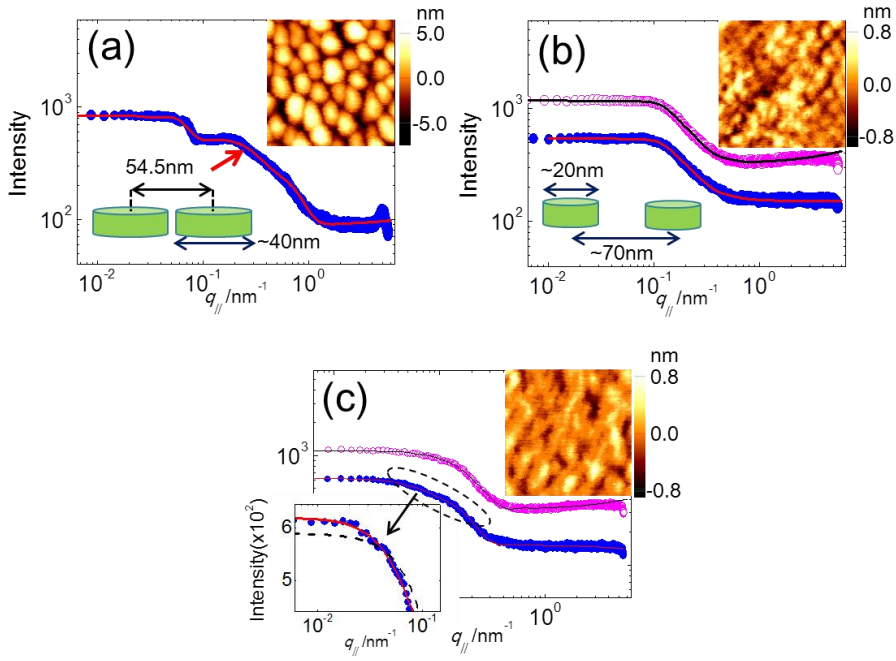

Figure 2.3(a), (b), (c) horizontal direction cuts of the 2D images and model fit result about CuPc 50nm, ATD CuPc|C_{60}, co-deposited CuPc:C_{60} (red open circles: 0.1° incident angle data, blue closed circles: 0.25° incident angle data, lines: fitting result). Data of CuPc 50nm and ATD were fitted using a disc model. In the case of co-deposited CuPc:C_{60}, it was fitted using both a disk and a sphere model as shown in the inset of (c) (black dotted line: disk model, red solid line: sphere model). The positions of the line cutting are marked as dotted lines in the images of Fig. 2.2 (b), (c) and (d). Inset: 250×250 nm^2 AFM images of (a) CuPc, (b) ATD CuPc|C_{60} and (c) co-deposited CuPc:C_{60}.

A single layer model on a silicon substrate was adopted in the analysis. The fitting curves of the reflectivity data are shown as solid lines and the resulting fitting parameters of the analysis are summarized in Table 2.1. The mass densities of the films were calculated using the refractive index[12].

The mass density of the 50 nm thick CuPc layer was 1.47 gcm^{-3}, which is lower than the mass density of 1.62 gcm^{-3} of the crystal α-CuPc layer[14]. This low mass density indicates that the thermally evaporated CuPc layer has a large number of defects such as grain boundaries and vacancies. The addition of C_{60} in the CuPc layer by ATD and co-deposition increases the mass density to 1.56 and 1.61 gcm^{-3}, respectively. The increased mass density by the incorporation of C_{60} implies that C_{60} molecules lead to denser packing of the constituent molecules by filling in the gaps between CuPc nano-crystals. It is interesting to note that the co-deposited film has a higher mass density and denser packing than the ATD film, probably due to the existence of voids in nanometer size in the ATD film.

Table 2.1 Parameters obtained from x-ray reflectivity curve analysis

	δ of refractive index	Film density[a][gcm^{-3}]	Substrate density[gcm^{-3}]	Film thickness [nm]	(200) lattice parameter [nm]	Surface roughness [nm]	Substrate roughness [nm]
CuPc 50nm	2.28×10^{-06}	1.47	2.32	45.3	1.296	2.5	0.65
ATD	2.43×10^{-06}	1.56	2.36	51.0	1.103	1.2	0.50
co-dep	2.51×10^{-06}	1.61	2.36	27.1	1.150	1.6	0.60
error	0.1×10^{-06}	0.03	0.03	0.1	0.002	0.1	0.03

[a] Density of CuPc crystal= 1.62 gcm^{-3}[14] , C_{60} = 1.65~1.68 gcm^{-3}[15,16]

It is interesting to note that the co-deposited film has a higher mass density and denser packing than the ATD film, probably due to the existence of voids in nanometer size in the ATD film. This must be related to the nanostructure of the films and will be discussed later. The peak displayed in the reflection curve of the CuPc film in Figure2.2a corresponds to the α-CuPc (200) peak with a lattice spacing of 1.296 nm, indicating that CuPc without C_{60} was grown to the α-CuPc phase which has the *C2/c* monoclinic structure with a lattice constant of 2.592 nm along the a-axis[17]. On the contrary, the broad humps shown in the ATD and co-deposited CuPc:C_{60} films indicate that the CuPc forms an amorphous structure or small nano-crystals in the range of a few nanometers in the vertical direction. The surface roughness of 50-nm-thick CuPc film was 2.5 nm, which is close to the RMS roughness of ~2 nm from the AFM measurement. The surface roughness was reduced by C_{60} incorporation to 1.2 nm and 1.6 nm in the ATD and co-deposited CuPc:C_{60} films, respectively.

The nano-structure of the CuPc, ATD CuPc|C_{60}, and co-deposited CuPc:C_{60} films were investigated using GISAXS, whose 2 dimensional (2D) images are displayed in Figure2.2b, c and d, respectively. The scattering image of the CuPc film shows two wings as shown in Figure2.2b. The average distance between the grains of the CuPc crystals

in the horizontal direction in the film was obtained from the peak positions [arrows in Figure2.2b and Figure 2.3a] in the wings along the q_y direction, and it turns out to be 54.5 nm, which is consistent with the average distance of ~50 nm in the AFM image shown in the inset of Figure2.3a. The form factor and the structure factor of the films were obtained from the data fitting of the variation of the scattering intensity in the transverse direction along q_y in the 2D data (red dashed lines in Figure2.2b, c, and d). The transverse data were obtained at the position far from $q_z=0$ to diminish the surface scattering effect. Scattering data near $q_z=0$ are complicated to analyze due to scattering from the surface of a film. The fitting results using GISAXS modeling[18-20] are displayed as the solid lines in Figure2.3a, b, and c for the CuPc, ATD and co-deposited CuPc:C_{60} films, respectively. In the case of the CuPc and ATD CuPc|C_{60} film, the data were well fitted by a disk model shown in the inset of Figure2.3a and b, which is described in Equation (2-1), where *V*, *R*, and *H* are volume, radius and height of the disk.

$$P(Q) = \int_0^{\pi/2} \sin\theta d\theta (V\Delta\rho)^2 \left\{ \frac{\sin[QH(\cos\theta)/2]}{QH(\cos\theta)/2} \frac{2J_1[QR\sin\theta]}{QR\sin\theta} \right\}^2 \quad (2\text{-}1)$$

P is the scattering intensity as a function of wave vector *Q* and $\Delta\rho$ is the difference in scattering length densities between the disk and the surrounding medium.The 50 nm thick CuPc film showed excellent fitting

by the disk model with the disk being 40(±3) nm in diameter and 4.0(±0.5) nm in height as shown in Figure2.3a. Figure2.3b displays two horizontal GISAXS line cuts at different incident angles of 0.1° and 0.25°. Since the total reflection angles of the ATD and co-deposited CuPc|C_{60} films are 0.126° and 0.128°, respectively, at an x-ray energy of 11.6 keV, by the relation $\theta_c = \sqrt{2\delta}$ [12], the x-ray signals from the surface region are dominant at the 0.1° incident angle, while signals from the bulk region are dominant at the 0.25° incident angle. As shown in Figure2.3b, the GISAXS line cuts from 0.1° (red circles) and 0.25° (blue circles) incident angles are all fitted by the disk model for the ATD CuPc|C_{60} film with excellent agreements. In the case of the 0.1° incident angle, the average diameter of the disk was 20.4(±0.4) nm and the height of the disk was 6.0(±0.2) nm. In the case of the 0.25° incident angle, the average diameter of the disk was also 20.4(±0.4) nm and the height of the disk was 4.0(±0.2) nm, indicating that the height of the disk gets higher as the growth proceeds. The disk shape seems to originate from the pristine CuPc and the diameter of the disk gets smaller than the CuPc film due to the hindrance of the growth associated with the existence of C_{60} by the ATD. In the AFM measurement, such grains are distinguished but with much

less contrast than the CuPc film at the surface of the ATD CuPc|C_{60} film, as shown in the inset of Figure2.3b.

On the contrary, the GISAXS data from the co-deposited CuPc:C_{60} film was not fitted by the disk model as shown by the dashed line in the inset of Figure2.3c, which is the best fit of the data using the disk model. Even though a sphere model fits better as shown in Figure2.3c (the red solid line), the fitting is unrealistic since the fitting was performed with a mixture of spheres with a diameter of 18.8(±0.2) nm and 36.0(±2.4) nm for the incident angle of 0.1°, and 16.6(±0.1) nm and 44.0(±0.4) nm for the incident angle of 0.25°, which are larger than the thickness (27 nm) of the film. This result indicates that more complicated model is needed to analyze co-deposited film. Despite the dimension problem of the sphere model in co-deposited films, it is indubitable that in the ATD film the original CuPc disk shape is maintained under incorporation of C_{60}, while it disappeared in the co-deposited film. Therefore, it seems that CuPc and C_{60} are not clearly phase separated in the co-deposited film.

Other evidence of the formation of the BHJs comes from the absorption spectrum. Figure2.4 shows the UV-VIS spectra of 50 nm-thick films of co-deposited CuPc:C_{60} (1:1, black square), ATD CuPc|C_{60} (1:1, red circle), and simulated homogeneous mixture of CuPc and C_{60} (blue triangle). The simulated absorption curve was obtained by the separate measurement of

the absorption coefficient of CuPc and C_{60} followed by the weighted average of the absorption coefficients assuming a homogeneous mixture of the constituent materials with no interaction ($\alpha_{cal} = 0.5\alpha_{CuPc} + 0.5\alpha_{C60}$). In the UV region (200~350 nm), the ATD and the co-deposited CuPc:C_{60} films show identical spectra, inferring that the ratios and the amount of CuPc and C_{60} are same in the both films. In contrast, the ATD film showed an absorption peak at 450 nm with an almost similar absorption intensity as the simulated absorption which is weak in the co-deposited film. This peak is known to have originated from the C_{60} aggregation[21]. The degree of the aggregation in the ATD film can be as much as in the pristine C_{60} films represented by almost the same intensity as the simulated one. In the co-deposited film, however, the peak is very weak, indicating that the C_{60} has been more aggregated in the ATD film than in the co-deposited film. Moreover the ATD film shows a much higher absorption intensity than the co-deposited films at the Q-band of CuPc. Stronger Q band absorption in the ATD film than the co-deposited film seems to be originated from the different orientation of the CuPc molecules in the films. Since the transition dipole of a CuPc molecule is located in the molecular plane, higher absorption indicates that the molecular planes are more inclined toward the substrate in the ATD film than the co-deposited film. This speculation is supported by the smaller

lattice constant of the (200) plane in the ATD film (1.103 nm) than the co-deposited film (1.150 nm) shown in Table 2.1. Different inclined angle of CuPc molecules in the aggregates will modify the intermolecular interaction in the dimers resulting in the slight shift in the absorption peak position in the ATD film from the co-deposited and the neat CuPc films, as manifested in the absorption spectra.

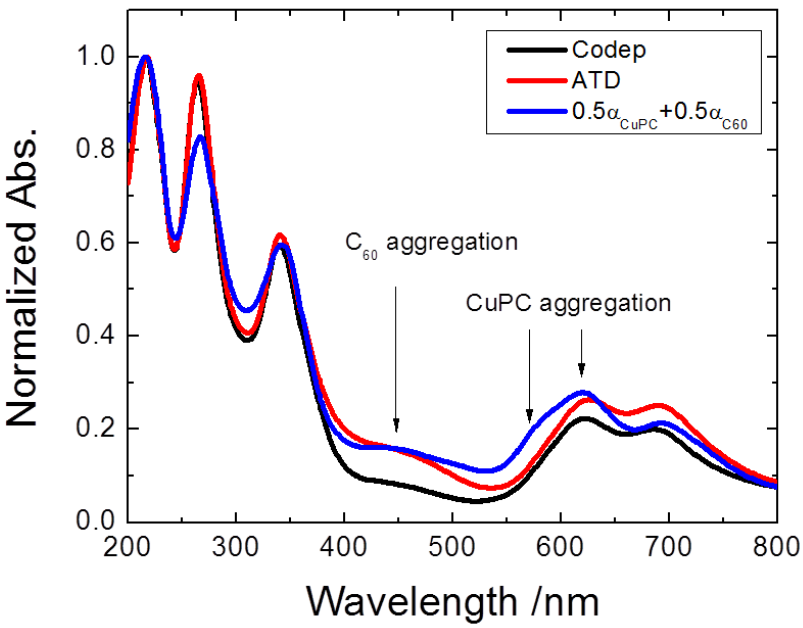

Figure 2.4 Measured UV-spectra of co-deposited (black) and ATD (red) films are compared to calculation (black) assuming a homogeneous mixture ($0.5\alpha_{CuPc}$ + $0.5\alpha_{C60}$) with no interaction. Arrows indicate the wavelength of CuPc and C_{60} aggregation absorptions.

The relative peak intensities between 620 nm (the absorption of H-type CuPc dimer) and 700 nm(the absorption of a CuPc monomer)[8] for the co-deposited and ATD films are similar in the absorption spectra. The nearly same relative peak intensities indicate that almost similar portion of CuPc molecules form dimers in the both films. The difference between the ATD and the co-deposited films seems to be located in the long range arrangement of the CuPc dimers. In the ATD films the CuPc dimers have ordering in the range of a few tens of nanometers. However, the dimers in the co-deposited film do not have long range ordering as shown by the GIWAXD results.

The difference in the nanostructure of the films will certainly influence the performance of the OSCs fabricated using the different deposition methods. Three devices were fabricated to demonstrate the difference; an ATD device [ITO/CuPc (3 nm)/ ATD CuPc|C_{60} (40 nm)/C_{60} (10 nm)/BCP (8 nm)/Al (100 nm)], a PHJ OSC [ITO/CuPc (20 nm)/C_{60} (40 nm)/BCP (8 nm)/Al (100 nm)] and a co-deposited OSC device [ITO/CuPc (3 nm)/ co-deposited CuPc:C_{60} (40 nm)/C_{60} (10 nm)/BCP (8 nm)/Al (100 nm)]. Figure 2.5 shows the current-voltage characteristics of the PHJ, co-deposited and ATD devices and the average characteristics of the OSCs taken from at least 4 devices for each type are summarized in Table 2.2. Compared with the PHJ device, the co-deposited device shows a

significant increase in J_{SC}, from 4.16 to 7.78 mAcm^{-2} due to the formation of a large number of interfaces helping with charge separation by co-deposition. Furthermore, a simple change of the co-deposited layer by the ATD layer increased the J_{SC}even more to 8.25 mAcm^{-2}. This increase of J_{SC} seems mainly due to higher molecular ordering in the ATD film resulting in efficient holes and electrons transport. In addition, the increase in fill factors (*FF*) of the ATD device (*FF* = 0.45) also supports that the ATD device can transport charges more efficiently than the co-deposited devices (*FF*=0.42). Saturated current densities at −1 V with illumination for the co-deposited and ATD devices are identical. This implies that the total numbers of excitons generated in both devices are same. However the ATD device shows more current at 0 V resulting from efficient charge transport. For the PHJ device, *FF* was 0.59, indicating that the ATD device still has room to improve. The overall performance of the device with the ATD layer was also enhanced showing a power conversion efficiency (*PCE*) of 1.53% compared to the co-deposited device (1.32%) and the PHJ device (1.10%). The V_{oc} value of the PHJ, co-deposited, and ATD devices was 0.44, 0.40, and 0.42V, respectively.

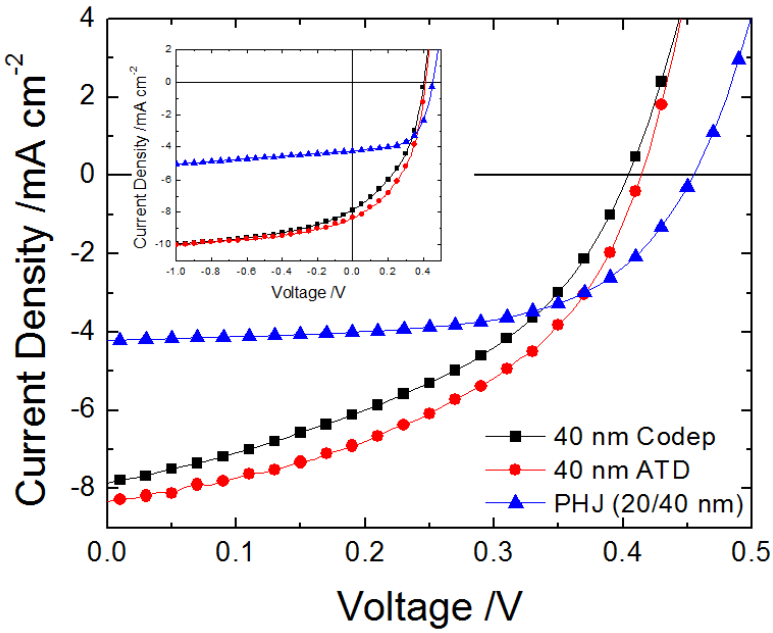

Figure 2.5J-V characteristics of PHJ (blue triangles) and BHJ OSC devices fabricated by ATD (red circles) and co-deposition (black squares) methods under AM 1.5 illumination. In the OSC device with ATD, J_{SC}, V_{OC}, *FF*, and PCE were 8.34 mA cm^{-2}, 0.41 V, 0.45, and 1.56%, respectively. Inset: J-V characteristics of the same figure with longer range.

Table 2.2 The power-conversion efficiency, PCE, short-circuit current, J_{SC}, open circuit voltage, V_{OC} and fill factor, *FF* of planar heterojunction (ITO/CuPc 20 nm/C_{60} 40 nm/BCP 8 nm/Al), PHJ, co-deposited (ITO/CuPc 3 nm/CuPc:C_{60} 1:1 40 nm/C_{60} 10 nm/BCP 8 nm/Al), and ATD (ITO/CuPc 3 nm/ATD CuPc|C_{60} 1:1 40 nm/C_{60} 10 nm/BCP 8 nm/Al)

	PCE [%]	J_{SC} [mA cm^{-2}]	V_{OC} [V]	FF
PHJ	1.10±0.09	4.16±0.21	0.44±0.01	0.59±0.01
co-dep	1.32±0.11	7.78±0.37	0.40±0.01	0.42±0.01
ATD	1.53±0.05	8.25±0.14	0.42±0.01	0.44±0.01

2.3.2 ZnPc and C_{60} system

CuPc|C_{60} showed improvement in performance in OSCs. Instead of CuPc, ZnPc is tested, which has the identical crystalline structure with CuPc when it is thermally evaporated on ITO or Si wafer substrate[22]. ZnPc is selected due to the crystalline structure and has been reported to show better performance than CuPc OSCs. To find out the effect of ATD, three devices were fabricated to demonstrate the difference; an ATD device [ITO/ZnPc (3 nm)/ ATD ZnPc|C_{60} (40 nm)/C_{60} (10 nm)/BCP (8 nm)/Al (100 nm)], a PHJ OSC [ITO/ZnPc (20 nm)/C_{60} (40 nm)/BCP (8 nm)/Al (100 nm)] and a co-deposited OSC device [ITO/ZnPc (3 nm)/ co-deposited ZnPc:C_{60} (40 nm)/C_{60} (10 nm)/BCP (8 nm)/Al (100 nm)]. Figure 2.6 shows the current-voltage characteristics of the OSCs listed above. Comparing with the PHJ device the co-deposited device shows a significant increase in J_{SC} from 5.37 to 9.06 mA cm^{-2} due to the formation of a large number of interfaces helping with charge separation by co-deposition as seen in CuPc systems. However comparing ATD OSCs with co-deposited OSCs the performance is not significantly enhanced showing 1.70% in PCE compared with 1.66% in co-deposited OSCs. Still the *FF* of ATD OSCs (0.43) showed better performance than co-deposited OSCs (0.37), inferring more effective charge-transporting network is formed.

J_{SC} showed similar values around 9.0 mA cm^{-2}. And the V_{OC} has decreased from 0.49 to 0.44.

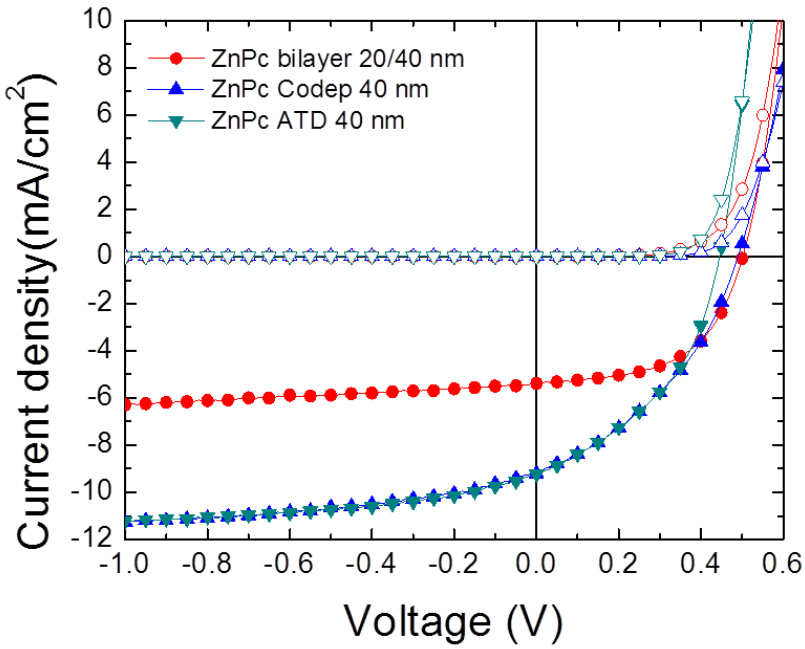

Figure 2.6 J-V characteristics of ZnPc-C_{60}PHJ (red circles) and BHJ OSCs fabricated by ATD (green triangles) and co-deposition (blue triangles) methods under AM 1.5 illumination.

To understand the difference between ZnPc and CuPc, the initial growth mode of ZnPc films is examined with GISAXS and GIWAXS. Figure 2.7a, b display the GIWAXS images of the 5 nm and 50 nm thick ZnPc and CuPc films grown on silicon wafers, respectively. The images clearly show the strong (200) diffraction peaks in the vertical direction, indicating that the ZnPc and CuPc films have preferred orientation with edge-on alignment of the molecules consistent with the previous reports [23,24].The (010) and (002) peaks are observed along the horizontal direction in the GIWAXS images as expected. Detailed information about the ZnPc crystals in the film were obtained by analysis of the GIWAXS images. The analysis results are shown in Figure 2.7c-e, which show the lattice parameters (Figure 2.7c), crystal domain size (Figure 2.7d), and angular spread of orientation of the ZnPc cystals (Figure 2.7e) in the films with different thicknesses. The lattice parameters a^* and b^* in Figure 2.7c are the normalized lattice parameters of the ZnPc films to those of the γ phase CuPc crystal whose parameters are a = 2.633 nm, b = 0.381 nm, and c = 2.371 nm and the β angle is 94.3°[24].The crystallographic detail information of the γ phase ZnPc crystal has not been reported yet. K. Leo's group adopted γ phase CuPc unit cell for γ phase ZnPc. The lattice parameters of the 5 nm thick ZnPc film in Figure 2.7c show that the lattice parameter a is larger and the lattice parameter b is smaller than

the values of the bulk, indicating that the ZnPc film at the initial growth region is under compressive stress in the lateral direction. The lattice parameter a decreased, whereas the lattice parameter b increased at the thickness of 10 nm, implying that the compressive strain relaxed at the thickness exceeding 10 nm. Still it is curious that both a^* and b^* are smaller than 1. This may come from the uncertainty of the lattice parameters of the γ phase ZnPc crystals.

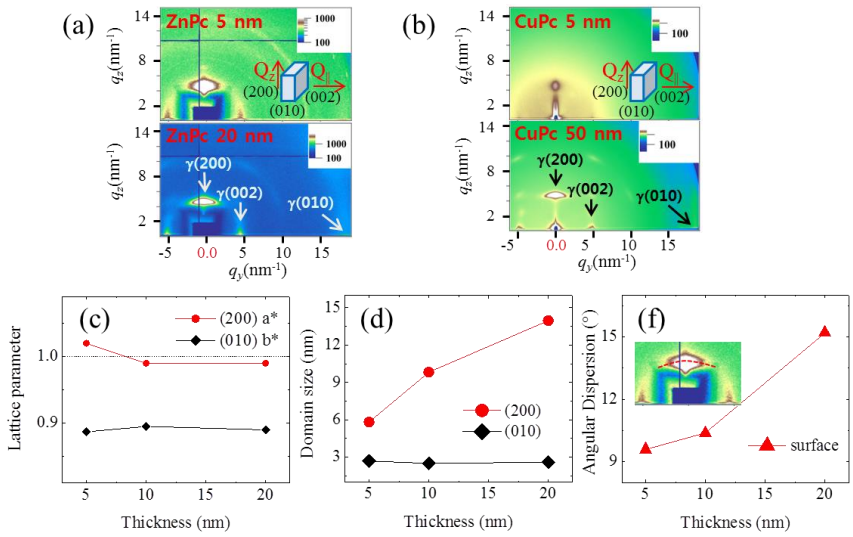

Figure 2.7 (a)(b) GIWAXS 2D images of the ZnPc and CuPc for 5 nm and 50 nm thick films, respectively; (c) The normalized lattice parameters, (d) crystal domain size, and (f) angular dispersion of γ-phase ZnPc as a function of the film thickness. The angular dispersion indicates the FWHM of the γ(200) peak in the circular direction, as shown in the dotted line in the inset (e). The peak positions of the (200), (002), and (010) orientation of the γ-phase are shown in the GIWAXS 2D diffraction images.

The changes in the lattice parameters can also be related to the variation of the tilt angle of the molecules because the tilt angle and the molecular conformation may also change during the growth [25]. The tilt of the organic molecules is related to the interaction energy between organic molecule and the substrate. The relaxed lattice parameter in the thin film should be measured to clarify the issue. The angular spread of the ZnPc films, which is related to the variation of the orientation among the crystals, increased with the film thickness as shown in Figure 2.7e. In contrast, the angular spread of the CuPc films did not increase with the increase of the film thickness up to 50 nm, and no strain relaxation was observed even in the 50 nm thick films. In addition an ultra-thin (5 nm) CuPc layer consisted of regularly ordered disk-type CuPc grains and the ordering was retained up to the CuPc film thickness of 50 nm. These behaviors of CuPc layer will be covered in Chapter 3. The initial growth mode of the ZnPc and CuPc layers are compared and analyzed using GISAXS shown in Figure 2.8. In contrast to the CuPc film, the 5 nm thick ZnPc film did not reveal a fine structure factor. Using IsGISAXS, the structure of ZnPc was fitted based on the ellipsoid nano-grains with 15 nm in diameter and 4.5 nm in height. For CuPc, a paracrystal model is adopted to fit the GISAXS data, showing that the diameter of CuPc grain is 16 nm and the height is 4 nm. The average distance of CuPc grains is

50 nm. These difference in initial growth between ZnPc and CuPc supports the hypothesis of the mechanism of formation of bulk heterojunction describe in Figure 2.1b that the surface control is an important factor.

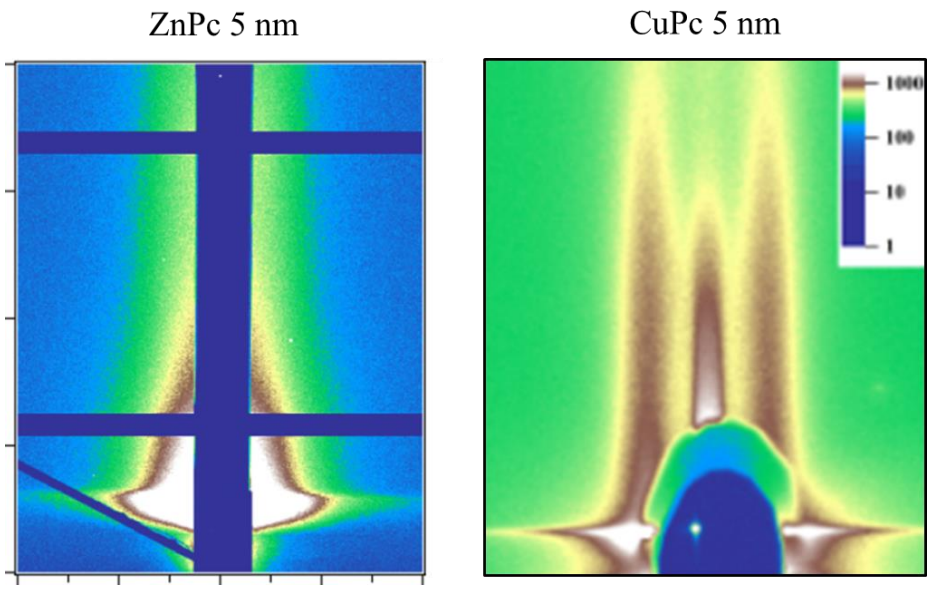

Figure 2.8 GISAXS images of ZnPc and CuPc for 5 nm.

The interaction energy differences between the following molecules are calcultated;CuPc-CuPc, ZnPc-ZnPc, CuPc-C_{60}, ZnPc-C_{60} and C_{60}-C_{60}. These calculations were done by Young Ho Kang in Prof. Seungwu Han's laboratory. Theoretically the binding energies between the small molecules are investigated using the VASP code which is based on the density functional theory (DFT)[26]. Generalized gradient approximation (GGA) is employed for exchange-correlation energy and the semi-empirical Grimme method [27] is used as the correction scheme of the long-range van der Waals interactions for the conventional Kohn-Sham DFT energy. The supercell size is determined for the distance between periodic images of the molecules to be large enough to minimize the interaction of the molecules of neighboring cells.

Two different binding geometries between two metal phthalocyanine (MPc) molecules were used as shown in Figure 2.9. It is found that the one in which the center of two molecules are slightly displaced (configuration 2) but no distorted is the most stable structures, which is more found in the MPc crystal structure. The distances with the minimum energies are 0.325nm, which is similar to the lattice parameter *b* of MPc, 0.381 nm, inferring this approach is reasonable. In addition, we also examined a variety of binding structures between C_{60} and MPc and it is

revealed that C_{60} located on the center of MPc is energetically favorable. We evaluate the binding energy (E_b) between two molecules as follows:

$$\mathrm{E}_b = (\mathrm{E}_{\mathrm{tot}} - \mathrm{n}(\mathrm{E}_{\mathrm{C60(PC)}} + \mathrm{E}_{\mathrm{PC}}))/\mathrm{n}$$

whereE_{tot}, E_{C60}, and E_{PC} are the total energy of complex structures, the energy of isolated C_{60} and MPc molecules, respectively. *n* represents the number of MPc and C_{60} in a supercell.

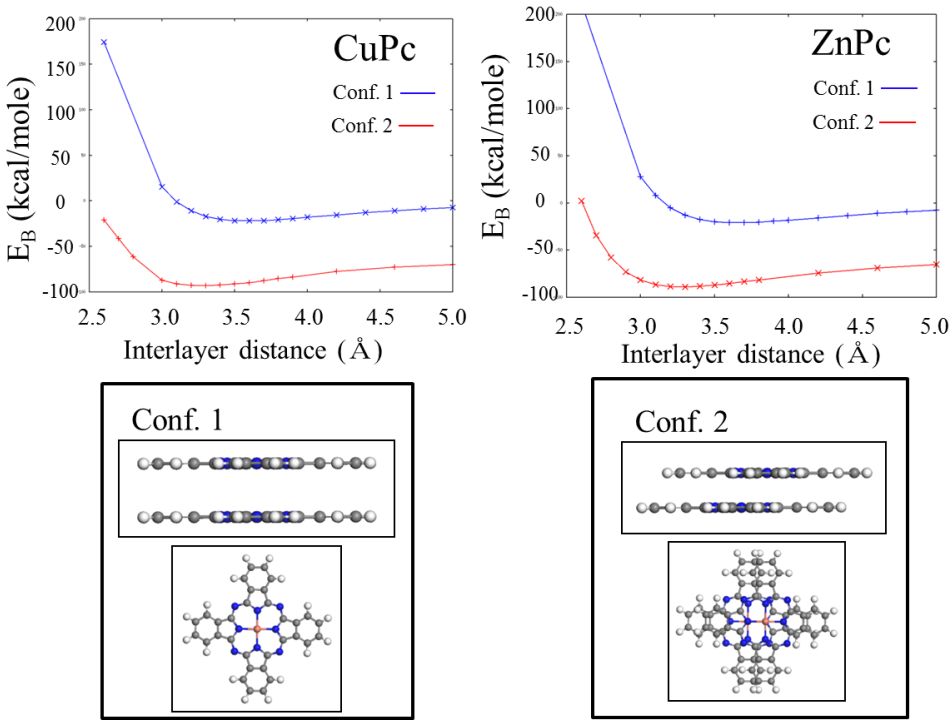

Figure 2.9 Binding energy vs intermolecular distance with two different configurations for ZnPc and CuPc.

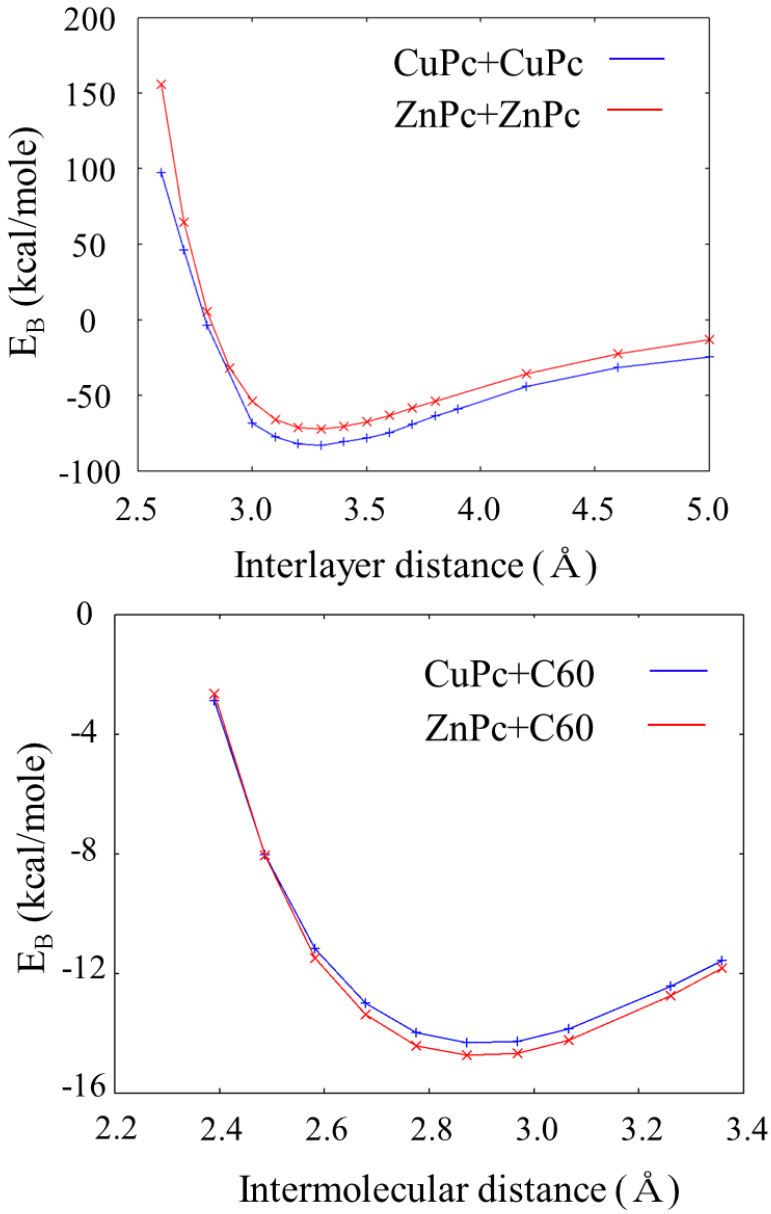

Figure 2.10 Binding energy vs intermolecular distance calculation result for CuPc-CuPc, ZnPc-ZnPc, CuPc-C_{60}, and ZnPc-C_{60}.

The binding energy of two CuPc molecules (93.2 kcal/mole, 4.04 eV) is larger than that of ZnPc molecules (88.7 kcal/mole, 3.85 eV). In case of the binding energies between MPcs and C_{60}, ZnPc showed slight more interactive with C_{60} (14.7 kcal/mole, 0.64 eV) than CuPc (14.3 kcal/mole, 0.62 eV). The values of the calculated energy for CuPc are different from the reported values [10], the trends were the same. From these calculations, it is found that CuPc molecules interact more with neighboring CuPc than C_{60} compared with that of ZnPc. In other words, CuPc molecules might aggregate more than ZnPc when it is deposited alternatively with C_{60}.

2.4 Conclusion

We formed BHJs using the ATD technique in small molecules and demonstrated efficient OSCs. GISAXS analysis showed that the ATD films consist of CuPc nano clusters with a disk shape (d = 20 nm, h = 6 nm). The absorption spectra of ATD films shows C_{60} aggregation, which infers ATD films form better BHJs than co-deposited films. The BHJs formed by ATD enhanced performances of OSCs by increasing the J_{SC}, *FF*, and *PCE* values. The ability of ATD to form the BHJs combined with its simplicity clearly demonstrates that the ATD is a promising technique to fabricate high efficiency small molecular OSC devices with a BHJ structure. However with ZnPc, OSCs with ATD did not showed great improvements, which can be understood with the difference in the growth mode at the initial state and in the interaction energy.

2.5 Bibliography

[1] C. Tang, *Appl. Phys. Lett.* **1986**, *48*, 183.

[2] J. Roncali,*Accounts of Chemical Research* **2009**, *42*, 1719–1730.

[3] L.-M. Chen, Z. Hong, G. Li, Y. Yang, *Advanced Materials* **2009**, *21*, 1434–1449.

[4] S. H. Park, A. Roy, S. Beaupré, S. Cho, N. Coates, J. S. Moon, D. Moses, M. Leclerc, K. Lee, A. J. Heeger, *Nature Photon* **2009**, *3*, 297–302.

[5] Do Young Kim, F. So, Y. Gao, *Solar Energy Materials and Solar Cells* **2009**, *93*, 1688–1691.

[6] Y. Terao, H. Sasabe, C. Adachi, *Appl. Phys. Lett.* **2007**, *90*, 103515.

[7] B. Walker, A. B. Tamayo, X.-D. Dang, J. H. Seo, A. Garcia, T.-Q.Nguyen, *Advanced Functional Materials* **2009**, *19*, 3063–3069.

[8] B. Rand, J. Xue, S. Uchida, S. Forrest, *Journal of Applied Physics* **2005**, *98*, 124902.

[9] P. Peumans, S. Uchida, S. Forrest, *Nature* **2003**, *425*, 158–162.

[10] F. Yang, K. Sun, S. R. Forrest, *Advanced Materials* **2007**, *19*, 4166–4171.

[11] M. Andreasson, L. Ilver, J. Kanski, T. Andersson, *Physica Scripta* **2006**, *2006*, 1.

[12] L. Parratt, *Phys. Rev.***1954**, *95*, 359–369.

[13] S. K. Sinha, E. B. Sirota, S. Garoff, *Phys Rev B***1988**, *38*, 2297–2311.

[14] K. Hayashi, *Physica B: Condensed Matter***2005**, *357*, 227–231.

[15] W. Krätschmer, L. Lamb, K. Fostiropoulos, D. Huffman, *Nature***1990**, *347*, 354.

[16] J. Kwiatkowski, J. Frost, J. Nelson, *Nano Letters***2009**, *9*, 1085–1090.

[17] O. Berger, W. Fischer, B. Adolphi, S. Tierbach, V. Melev, J. Schreiber, *Journal of Materials Science: Materials in Electronics***2000**, *11*, 331–346.

[18] D. Kinning, E. Thomas, *MACROMOLECULES***1984**, *17*, 1712–1718.

[19] R.-J. Roe, *Methods of X-Ray and Neutron Scattering in Polymer Science*, Oxford University Press, New York, **2000**.

[20] A. Nelson, T. Cosgrove, *Langmuir***2004**, *20*, 2298–2304.

[21] R. Bensasson, E. Bienvenue, M. Dellinger, S. Leach, P. Seta, *The Journal of Physical Chemistry***1994**, *98*, 3492–3500.

[22] H. J. Kim, J. W. Kim, H. H. Lee, B. Lee, J.-J. Kim,*Advanced Functional Materials***2012**, *22*, 4244–4248.

[23] H. J. Kim, J. W. Kim, H. H. Lee, T.-M. Kim, J. Jang, J.-J. Kim, *J.*

*Phys. Chem. Lett.***2011**, 1710–1714.

[24] C. Schuenemann, C. Elschner, A. A. Levin, M. Levichkova, K. Leo, M. Riede, *Thin Solid Films***2011**, *519*, 3939–3945.

[25] S. Kowarik, A. Gerlach, F. Schreiber, *J Phys-Condens Mat***2008**, *20*, 184005.

[26] G. Kresse, *Phys Rev B***1996**, *54*, 11169–11186.

[27] S. Grimme, *J. Comput. Chem.***2006**, *27*, 1787–1799.

Chapter 3. Initial Growth of planar organic molecules affected by substrate surface energy

3.1 Introduction

Copper(II) phthalocyanine (CuPc) is an archetype planar molecule which is used as a donor material in small molecular bulk heterojunction (BHJ) organic solar cells. As observed in Chapter 2, formation of the BHJs with interpenetrating network with ATD seems to be affected by the initial growth of the molecules. The mixed structure is fabricated by simple thermal co-deposition of donors and acceptors or controlled organic molecular beam deposition which is based on the evaporation of molecules in a vacuum[1-4].In a vacuum deposition, the morphology of a layer is affected by growth conditions such as the deposition rate, the temperature of a substrate, the surface state of a substrate, etc. Among various parameters, the surface free energy of a substrate significantly affects the growth mode of the organic layers[5-7].When the surface free energy of the substrate is higher than the surface free energy of the film and interface, the organic molecules grow following a layer-by-layer growth mode. On the other hand, the island growth mode is dominant when the surface free energy of a substrate is lower than the surface free energy of the film and the interface.

For instance, the CuPc morphology is column like on a low energy surface because the low surface energy results in weak interactions between the molecule and the substrate favoring the stacking of molecules on molecules rather than on the surface. In contrast, CuPc is horizontally aligned and tends to cover the whole substrate surface to reduce the total surface energy. This phenomenon was observed on various substrates such as SiO_2, Au, ITO, SAM treated surfaces[8-11].

Despite well-known previous results on CuPc films, the morphology and the orientation of CuPc molecules at the initial growth regime is not clear yet. At the initial growth regime, the strain relaxes to transform from the surface structure to its bulk structure within 1 ~ 5 monolayers [12]. Since the initial growth mode dictates the further growth, the behavior of the morphology of the initial growth regime is important in thin film systems. The most morphological studies of the initial ultra-thin films were done by AFM or TEM measurement [8-11]. AFM or TEM measurement is useful to investigate surface morphology in organic films, but it does not supply the information about molecular orientation. The molecular orientation is generally studied by x-ray diffraction (XRD) measurement, but conventional XRD is not proper in the ultra-thin organic layer due to a small scattering cross section of organic materials.

Synchrotron x-rays are used for the investigation of systems with a small scattering cross section [13-15].

In this study, for the first time detailed structures of the initial ultra-thin (~ 4 monolayers) CuPc layer grown on differently treated Si substrates to have different surface energies are studied. The crystalline structure was obtained by the grazing incidence small angle x-ray scattering (GISAXS) and grazing incidence wide angle x-ray scattering (GIWAXS) measurement. The results show that CuPc grows in disc type nano grains with high crystalline ordering on a high surface energy Si surface. On a low surface energy Si surface, however, the nano grains do not exist with low crystalline ordering. Based on the analysis of the GISAXS and GIWAXS data, the models of the CuPc layer on high surface energy as well as on low surface energy Si surfaces is proposed. The FET mobility also supports our models.

3.2 Experiments

A high surface energy Si surface and a low surface energy Si surface is prepared by Piranha (H_2SO_4:H_2O_2=4:1 mixed solution) and octadecyltrichlorosilane (ODTS) treatments, respectively. The surface energy was 79.04 mN/m for a Piranha treated Si surface, while it was 32.9 mN/m for an ODTS treated Si surface. The surface energy of silicon was obtained by a contact angle measurement with the FOWKES and WU methods.

Atomic force microscope (AFM) topographic and phase images of 5 nm thick CuPc films on Piranha treated or ODTS treated Si wafers were taken using a PSIA XE-100 scanning probe microscope with the non-contact mode. The CuPc films are thermally deposited under a vacuum of 10^{-7} torr.

GIWAXS, GISAXS and x-ray reflectivity were measured at the 5A beam line of the Pohang Light Source of Korea. The x-ray energy was 11.6 keV. The distance from the sample to the detector was 57 cm in the GIWAXS measurement, and it was 2 m in the GISAXS measurement. In the GIWAXS measurement, a 2D image detector covered up to 1.5 $Å^{-1}$ in reciprocal space, which corresponds to ~4.19 Å in real space.

The mobility of CuPc was measured with field-effect transistor (FET) devices. Top-contact FETs were fabricated on heavily doped (n^{++}) silicon

wafer which works as the common gate electrode. Thermally grown SiO_2 (100 nm) was used for a gate dielectric insulator. The SiO_2 surface was modified with Piranha treatment and ODTS treatment. Temperature dependency of FET mobility is measured on a copper cold chuck using a liquid nitrogen flow for cooling and a heater to maintain the temperature. CuPc (40 nm) film was deposited with thermal evaporation under a pressure of 10^{-7} torr. The Au electrode (50 nm) was deposited by thermal evaporation and the source and drain electrodes are patterned with a metal shadow mask. The channel length and width were defined to be 60 μm and 500 μm, respectively. Electrical characteristics were measured with an Agilent 4155C semiconductor parameter analyzer in a vacuum chamber.

3.3 Results and discussion

Figure3.1 shows the transfer characteristics of the CuPc FETs. The mobilities obtained from the transfer curves are 2×10^{-5} $cm^2/V\cdot s$ on the hydrophilic surface and 2.5×10^{-4} $cm^2/V\cdot s$ on the hydrophobic surface, respectively.

Figure 3.2 shows the AFM images of a 5 nm thick CuPc layer on high surface energy Si (Piranha treated) as well as on low surface energy Si (ODTS treated), respectively. The top row in Figure 3.2 is topography images of 1.0×0.5 μm^2, and the bottom row is phase images of the same area. The roughness of the CuPc on the low surface energy Si is 0.51 nm, which is larger than on the high surface energy Si, 0.24 nm. The CuPc film grown on the Piranha treated high energy surface shows a flat surface, however, the phase difference was larger than that on the ODTS treated surface. Comparing with the mobility of FET devices, the charge mobility seems to be more affected by the phase difference than the flatness of a CuPc surface. The phase difference originating from the density difference of CuPc or grain boundaries shows that the CuPc on high surface energy Si has bigger grain or nano cluster whose size of around 30 nm. The detail information about two films was obtained by GISAXS measurement.

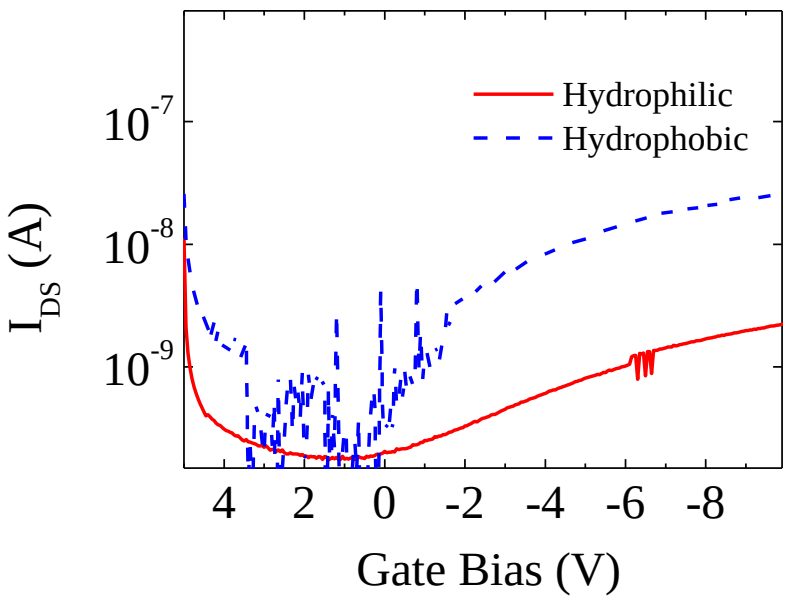

Figure 3.1 Transfer characteristics of CuPc OFET on a hydrophilic substrate (red line) and on hydrophobic substrate (blue line).

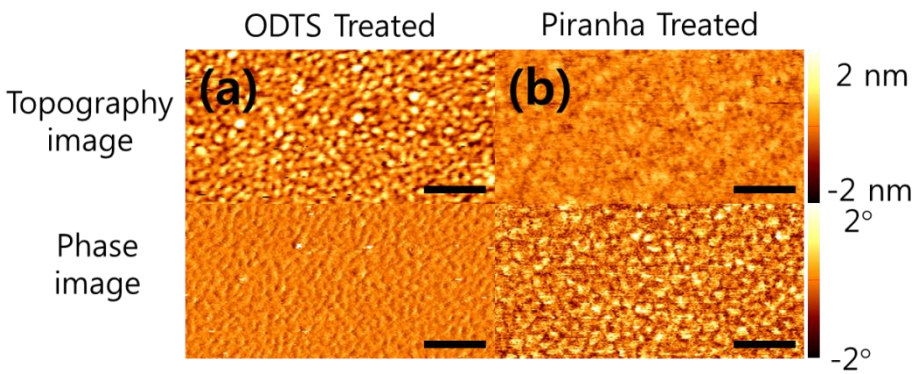

Figure 3.2AFM images of (a) CuPc on a hydrophobic (ODTS treated) surface and (b) hydrophilic (Piranha treated) on surface. The R_{rms} roughness of ODTS treated surface is 0.51 nm, while R_{rms} of the Piranha treated surface is 0.25 nm, respectively. (scale bar: 200nm)

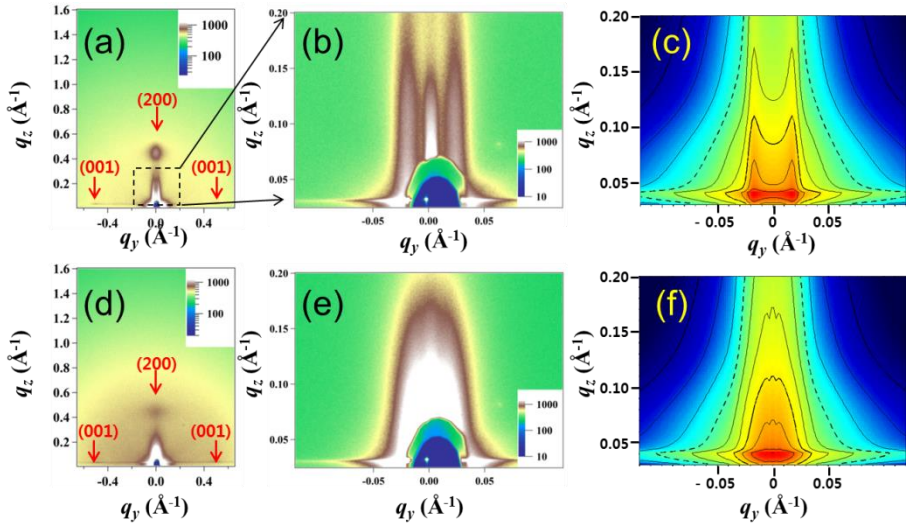

Figure 3.3(a) and (b) are measured GIWAXS and GISAXS images of a CuPc layer (5 nm) on a hydrophilic Si surface, respectively. (c) is a GISAXS simulation image using a disc type structure factor. The central rod originated from the specular scattering is not calculated in SAXS simulation. The two wings of SAXS pattern are originated from the interference between nano discs. (d) and (e) are GIWAXS and GISAXS images of a CuPc layer (5 nm) on an ODTS treated hydrophobic Si surface, respectively. (f) is a GISAXS simulation image of CuPc layer on an ODTS treated hydrophobic Si surface. Comparing to (c), the central rod is shown due to large disordering of the interference between nano dics.

Figure 3.3a and b display the GIWAXS and GISAXS images of an about 5 nm thick CuPc layer on the high surface energy Si. As shown in Figure3.3a, the CuPc molecules are stacked with a (200) preferred orientation by a showing strong (200) diffraction spot in the vertical direction. (001) peaks are shown in the horizontal direction. In this stacking, CuPc molecular planes are standing inclined 26.5° from the surface normal and Cu atoms centered in the molecular plane are aligned along the *b* axis [16,17]. The lattice parameters in the (200) and (001) directions are 1.34 nm and 1.25 nm, respectively. The lattice constants of crystalline bulk CuPc are 2.592 nm and 1.196 nm in (100) and (001). Comparing to the lattice constants of the bulk CuPc, it seems that CuPc unit cell is expanded in (100) and (001) in the ultra-thin film due to strain between the substrate. The crystalline size obtained from the full width at half maximum of the (200) and (001) peaks are 5.3 nm and 11.4 nm, respectively. Comparing the film thickness and the lattice parameters, CuPc molecules are regularly stacked to form crystals in the vertical direction, and 4~5 molecules are regularly stacked in the horizontal direction. The angular dispersion of the CuPc (200) peak is 8.36°, indicating that the nano-sized CuPc crystals are aligned preferentially in the (200) direction. As shown in GIWAXS image, the higher order peaks

of CuPc are not shown due to the small correlation by small sized CuPc grains.

The interesting point of GIWAXS results is the splitting of the central diffraction rod in the low q_z region, as shown in the dotted box in Figure3.3a. The splitting is more definitely shown in the GISAXS images as shown in Figure3.3b. The split rods of the central diffraction are originated from a structure factor in the GISAXS measurement, and the structure factor can be obtained by data simulation with theoretical modeling [18-21]. The GISAXS data modeling are done with a paracrystal model using IsGISAXS program [20]. The calculation is based on DWBA (Distorted wave Born approximation) theory. By the simulation, we found that CuPc film was consisted of disc type nano grains and the two intensity streaks of CuPc were originated from the interference of CuPc nano grains. The average diameter and the height of the disc were ~22 nm and ~4 nm, respectively. The average distance between the discs is ~30 nm. Figure3.3c shows the simulation result. In the simulation, the central rod is not shown because the central rod is mostly originated from the specular reflection at the surface. The specular signal in SAXS simulation is not calculated. In the calculation, σ_R/R, σ_H/H, and ω/D are all 0.35, 0.35 and 0.30 respectively. It is interesting to note that the size of the disc is much larger than the crystalline size

obtained from the diffraction images. This fact indicates that the discs are composed of the crystalline part and disordered region or multicrystallines with different *c*-orientations.

Figure3.3d and e exhibit the GIWAXS and GISAXS images of an about 5 nm thick CuPc layer on low surface energy Si, which is hydrophobic by ODTS treatment. Comparing with Figure3.3a, the diffraction peaks are weak and broad. The lattice parameters in the <200> and <001> directions are 1.41 nm and 1.28 nm, respectively. Comparing to the high surface energy Si, the lattice parameters are expanded more on the low surface energy Si in the ultra-thin layer. Interesting point is that lattice parameters are expanded in the vertical direction (lattice parameter *a*) as well as in the horizontal direction (lattice parameter *c*) regardless of the substrate surface energy. Generally, if one of them is expanded, the other is contacted to keep the volume. In case of CuPc, it seems that lattice parameter of *b* is contracted, while lattice parameters of *a* and *c* are expanded. Unfortunately, lattice parameter of *b* was not measured in our measurements. On a hydrophobic surface, ~7 CuPc molecules (~9.3 nm crystal size) are regularly stacked in the *c*-direction. The angular dispersion of the CuPc (200) peak is 23.6°. The lower intensity and larger angular dispersion of the (200) peak suggests that CuPc crystals are more randomly distributed on a hydrophobic surface than on a hydrophilic

surface. The more random distribution of CuPc nano grains was also confirmed by the GISAXS measurement. Figure3.3f is the simulation of GISAXS images of CuPc on an ODTS treated hydrophobic Si surface. We also adopted paracrystal model, and the results show that the diameter of CuPc is ~16 nm and the height is ~ 4nm. The average distance of CuPc grains is ~50 nm. Comparing to Figure3.3c, the central rod is shown in Figure3.3f due to the less periodically separated nano grains on an ODTS treated hydrophobic surface than on the hydrophilic surface. In the simulation, the σ_R/R and σ_H/H are all 0.35, and ω/D is 1.00 on an ODTS treated surface. Due to the large ω/D, form factor appears at the central region even in the paracrystal interference model. In order to obtain the average mass density of the films, we performed the x-ray reflectivity measurement shown in Figure 3.4. The x-ray reflectivity data was fitted by the following modeling. In case of CuPc film on a hydrophilic surface, the data could be fitted by single layer model. On the other hand, x-ray reflectivity data about CuPc film on the ODTS treated surface was fitted by two layer model including an ODTS layer. The density of ODTS layer was 0.98 g/cm^3, which is consistent to the reported values (0.9~1.05 g/cm^3) [22]. On a hydrophilic surface, the electron mass density CuPc layer was 1.49 g/cm^3. On the other hand, the electron mass density CuPc layer was 1.61 g/cm^3 on a hydrophobic surface, which is larger than that

on a hydrophilic surface and close to that of the CuPc bulk crystal (1.65 g/cm^3). The lower mass density in the film with better crystallity grown on the hydrophilic surface than the film grown on the hydrophobic surface can be understood by the discontinuous grains and existence of voids.

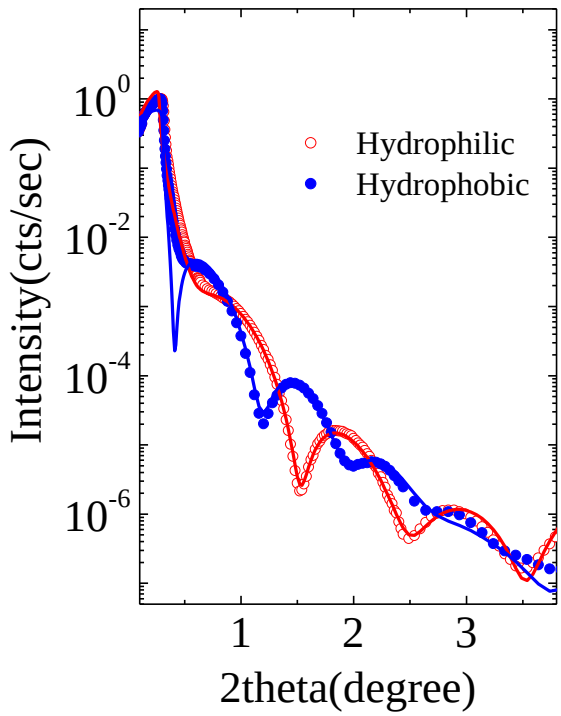

Figure 3.4 The x-ray reflectivity measurement for CuPc film on a hydrophilic surface (red open circle) and on a ODTS (hydrophobic) surface (blue closed circle). Solid lines indicates fitting.

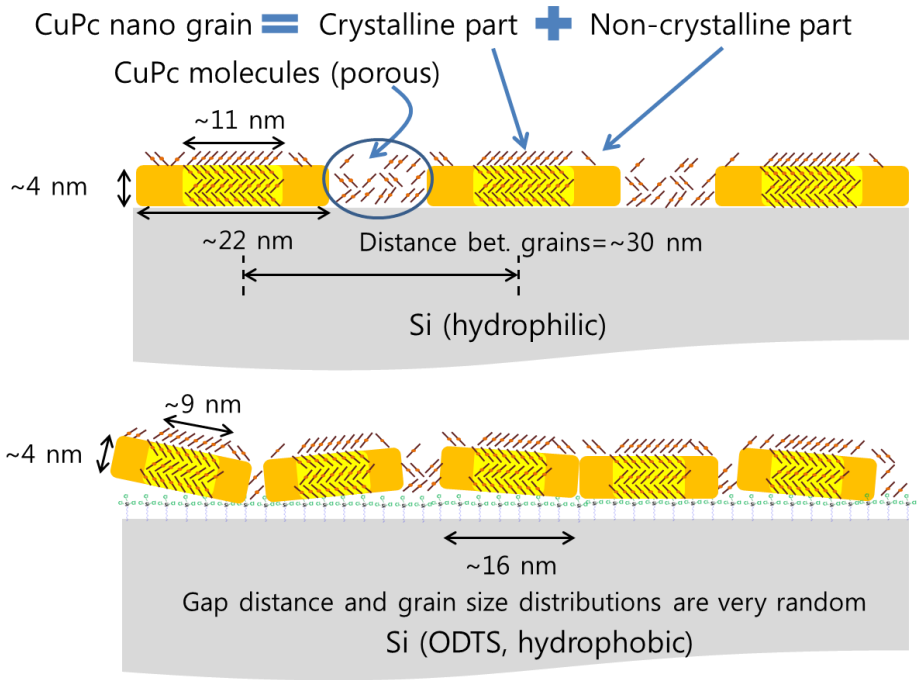

Figure 3.5 Model of CuPc ultra-thin layers on a hydrophilic surface and on a hydrophobic surface

Based on the structural information, we propose a model representing the structure of the CuPc thin films at the initial growth regime, which is schematically shown Figure 3.5. On the hydrophilic surface, CuPc molecules are packed forming nano discs, and the molecules are regularly stacked inside each disc. Even though the details between the discs are not clear, it seems that the gaps consist of pores and sparsely distributed CuPc molecules. On a hydrophobic surface, the CuPc molecules are stacked more randomly with a low crystallinity in comparison with the CuPc layer on a hydrophilic surface. Based on the SAXS calculation, the average distance of CuPc is larger on an ODTS treated surface than on the hydrophilic surface. But, the ω/D is almost 3 times larger than on the hydrophilic surface, which means 3 times large dispersion of distance between CuPc grain. AFM topography image also supports very random distribution of size and distance of CuPc grains on an ODTS treated surface. Therefore, smaller CuPc grains cover the ODTS treated surface with more random distribution with higher packing.

This model is supported by the charge carrier mobility in CuPc based FET devices fabricated on the hydrophilic and hydrophobic surfaces. As previously mentioned, the mobility of CuPc FETs is 10 time higher on a hydrophobic surface than on a hydrophilic surface. More densely packed CuPc molecules in average on the hydrophobic surface than the film on

the hydrophilic surface naturally give higher mobility in the FET on a hydrophobic surface than on a hydrophilic surface even though the crystalline portion is larger on the hydrophilic surface. The temperature dependence of the FET mobilities on the hydrophilic surfaces simply follows the Arrhenius relationship up to 180℃ as shown in Figure 3.6, indicating that it is thermally activated process. On the other hand, the mobility on the hydrophobic surface shows lower activation energy compared to that of OFET on hydrophilic surface below 100℃, supporting the proposed model that the gap between the gain is larger in the hydrophilic surface.

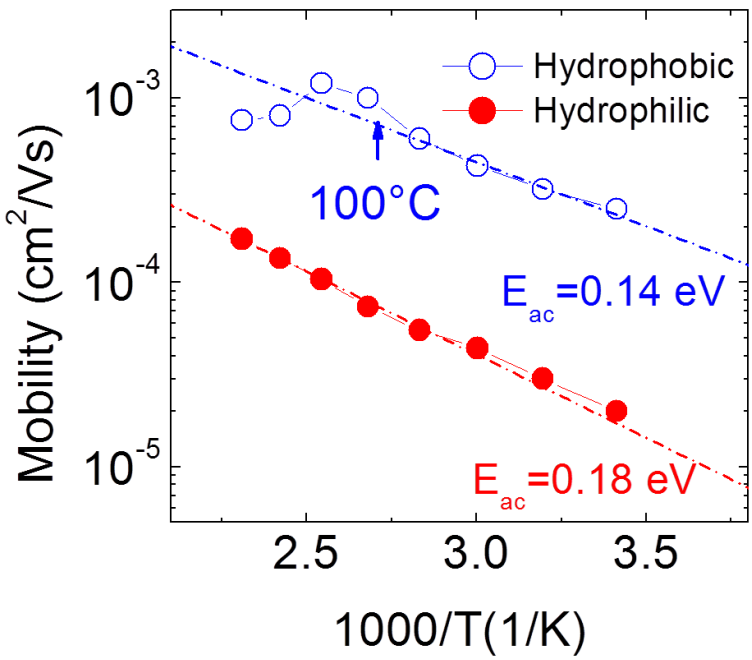

Figure 3.6 Temperature dependence of mobilities of OFET devices fabricated on a hydrophilic surface and a hydrophobic surface.

The FET mobility on hydrophobic surface undergoes increase and decrease above 100℃. These phenomena can be understood with the thermal evolution of the nano-sturctures. This detailed study is reported in *Journal of Materials Chemistry* (2012) 22, 8881.

Despite the low FET mobility, the nano disc shape of CuPc on a hydrophilic surface with voids between disc shaped grains can be advantageous in OPVs. As previously mentioned, CuPc is used as a donor material in mixed BHJ OPVs. Therefore, the basic property of CuPc nano discs on a hydrophilic surface implies that CuPc is favorable to form BHJs in small molecular OPVs. This must be a reason that the co-deposition of CuPc and acceptor molecule increases the power conversion efficiency significantly than the layered structure.

3.4 Conclusion

Disc type nano grains of CuPc were observed in an ultra-thin CuPc layer (5 nm) evaporated on a hydrophilic Si surface showing the structure factor in grazing incidence small angle x-ray scattering measurement. The disc type grains consisted of a crystalline part and a non-crystalline part. The disc type grains were smaller in the case of evaporation on an ODTS treated hydrophobic Si surface, which showed lower crystallinity with random distribution. Despite regularly distributed CuPc grains, the mobility was lower in a FET device fabricated on a hydrophilic surface than on an ODTS Si surface due to the lower average density of the molecules relating to porous molecular packing between nano grains on a hydrophilic surface

3.5 Bibliography

[1] P. Peumans, S. Uchida, S. R. Forrest, *Nature* 2003, **425**, 158-162.

[2] F. Yang, K. Sun, S. R. Forrest, *Adv. Mater.* 2007, **19**, 4166-4171.

[3] H. X. Wei, J. Li, Z. Q. Xu, Y. Cai, J. X. Tang, Y. Q. Li, *Appl. Phys. Lett.* 2010, **97**, 083302-083304.

[4] J. W. Kim, H. J. Kim, H. H. Lee, T. Kim, J.-J. Kim, *Adv. Funct. Mater.* 2011, **21**, 2067-2071

[5] D. J. Eaglesham, M. Cerullo, *Phys. Rev. Lett.* 1990, **64**, 1943-1946.

[6] R. Ruiz, *Chem. Mater.* 2004, **16**, 4497-4508.

[7] S. Karan, B. Mallik, *J. Phys. Chem. C* 2007, **111**, 7352-7365.

[8] K. Xiao, Y. Liu, G. Yum, P. Zhu, *Appl. Phys. A* 2003, **77**, 367-370.

[9] S.-C. Suen, W.-T.Whang, F.-T.Hou, B.-T. Dai, *Org. Electron.* 2006, **7**, 428-434.

[10] S. Khodabakhsh, B. M. Sanderson, J. Nelson, T. S. Jones, *Adv. Funct. Mater.* 2006, **16**, 95-100.

[11] Y.-S. Hsiao, W.-T.Whang, S.-C.Suen, J.-Y.Shiu, C.-P.Chen, *Nanotechnology* 2008, **19**, 415603.

[12] S. R. Forrest, *Chem. Rev.* 1997, **97**, 1793-1896.

[13] D. Vaknin, W. Bu, *J. Phys. Chem. Lett.* 2010, **1**, 1936-1940

[14] X. Mulet, D. F. Kennedy,T. L. Greaves, L. J. Waddington, L. J., A. Hawley, N. Kirby, C. J. Drummond, *J. Phys. Chem. Lett.* 2010, **1**, 2651-2654

[15] N. Javid, K. Vogtt, S. Roy, A. R. Hirst, A. Hoell, I. W. Hamley, R. V. Ulijn, J. Sefcik, *J. Phys. Chem. Lett.* 2011, **2**, 1395-1399

[16] C. J. Brown, *J. Chem. Soc. A* 1968, 2488-2493.

[17] O. Berger, W.-J. Fisher, B. Adolpi, S. Tierbach, V. Melev, J. S. Schreiber, *J. of Mater. Sci.: Mater. Electron.* 2000, **11**, 331-346.

[18] T. Salditt, T. H. Metzger, J. Peisl, B. Reinker, M. Moske, K. Samwer, *Europhys. Lett.* 1995, **32**, 331-336.

[19] R. J. Roe, Oxford University Press: New York Oxford, 2000.

[20] R. Lazzari, R. *J. Appl. Cryst.* 2002, **35**, 406-421.

[21] P. Müller-Buschbaum, *Anal. Bioanal. Chem.* 2003, **376**, 3-10.

[22] A. G. Richter, C.-J. Yu, A. Datta, J. Kmetko, P, Dutta, *Phys. Rev. E.* 2000, **61**, 607-615

Chapter 4. High performance organic planar hetero-junction solar cells by controlling the molecular orientation

4.1 Introduction

The control of molecular orientation is an important research topic in organic electronics at the present time because the electrical and optical properties of a molecular film are significantly influenced by the molecular orientation in the film [1-3]. Organic solar cells (OSCs) are not an exception. To enhance the power conversion efficiency (PCE), the short circuit current (J_{SC}), open circuit voltage (V_{OC}), and fill factor (FF) need to be increased. These three terms are closely related to the molecular orientations of donor and acceptor materials. By matching the molecular transition dipole moment to the electric field of incident light, the total amount of absorption within the exciton diffusion length can be enhanced, resulting in the increase of the J_{SC} value. V_{OC} is closely related to the energy difference between the highest occupied molecular orbital (HOMO) of the donor and the lowest unoccupied molecular orbital (LUMO) [4-5]. The well-ordered molecular orientation affects not only these HOMO-LUMO energy levels but also the ionization potentials (IP) in organic thin films [1,6,7]. In addition to the change in IPs, the strength of their interface dipoles and the resulting band alignments at the organic-

organic interfaces are also affected in accordance with the molecular orientation [8]. High electron and hole mobilities are required to achieve a high *FF* favoring the face-on packing of molecules along with high crystallinity. In most cases, metal phthalocyanines (MPcs) grow with edge-on orientations when they are thermally deposited on ITO or SiO_2 substrates [9-11,13]. The edge-on orientation is unfavorable for light absorption and charge transportation. Therefore controlling the crystallinity and the orientation of MPcs toward a face-on orientation is important for improving the performance of OSCs. This molecular orientation control was successfully demonstrated by introducing copper iodide (CuI) layer to copper phthalocyanine (CuPc) [11] and lead phthalocyanine (PbPc) [12] resulting enhancement in PCE.

Here we report a highly efficient planar heterojunction OSC based on zinc phthalocyanine (ZnPc)/fullerene (C_{60}) with 2.7 times enhancement by controlling the orientation of the ZnPc by CuI as the interfacial layer between indium tin oxide (ITO) and ZnPc. The molecular orientations were analyzed with wide angle x-ray scattering (WAXS) and optical absorption, confirming that the proportion of ZnPc molecules with a face-on orientation was increased significantly on the CuI layer. Not only the absorption but V_{OC} also has increased. The PCE of the orientation controlled planar heterojunction OSC was remarkably enhanced to

3.2±0.1% compared with 1.2±0.1% of the conventional OSCs without the molecular orientation. The V_{OC} enhancement is discussed via the results of the ultraviolet photoemission spectra (UPS) measurements.

4.2 Experiments

For OSCs fabrication, the ITO-coated glass substrates were cleaned with acetone and isopropyl alcohol. The substrates were exposed to UV–O_3 for 10 min before use. CuI, ZnPc, C_{60}, 2,9-dimethyl-4,7-dipheyl-1,10-phenanthroline (BCP) and Al were thermally deposited under a vacuum of 10^{-7} torr. All layers except CuI layer were successively evaporated without breaking the vacuum and all devices were encapsulated in ambient N_2 before photocurrent measurements. The substrates were kept at room temperature during the evaporation process. The active areas were 4 mm^2. The photocurrents were measured under illumination from an AM1.5 solar simulator (300W Oriel 91160A). The light intensity was carefully calibrated using a standard silicon solar cell (NREL). A Keithley 237 source measurement unit was used for measuring current density–voltage characteristics.

The UV-VIS absorption spectra of studied films were recorded with a VARIAN Cary 5000 UV-Vis spectrophotometer. All films were thermally evaporated on clean quartz substrates.

GIWAXS (grazing incidence wide angle x-ray scattering) measurements were performed at station 12IDB and 12IDC of the Advanced Photon Source (APS). The x-ray energy was 12 keV. The distance from the

sample to detector was 227 mm, and a 2D CCD detector PILATUS 2M (pixel size is 2 M) was used for GIWAXS measurements.

The UPS experiments were carried out in an ultrahigh vacuum chamber connected to a preparation chamber where all the deposition processes and UV:O_3 treatment took place. Spectra were recorded on a VG ESCALAB 220i system using a He I (21.2 eV) source for UPS. The base pressures of the preparation chamber and the analysis chamber were 7×10^{-9} and 2×10^{-10} torr, respectively. The UPS spectra were recorded with a sample bias of -10 V for WF measurements and 0 V for VB measurements. Energy resolutions were approximately 0.1 eV.

4.3 Results and discussion

4.3.1 ZnPc planar heterojunction OSCs

Figure 4.1 shows the representative current density-voltage characteristics of the ZnPc based planar heterojunction OSCs with or without CuI under AM 1.5 solar simulator illuminations. The device with the structure of ITO/CuI 3 nm/ZnPc 25 nm/C_{60} 40 nm/BCP 8 nm/Al 100 nm is compared with the control device without the CuI layer. CuI is used as an interfacial layer to control the orientation of the ZnPc molecules [11,12,14] and the BCP layer is used as an exciton blocking layer. By inserting the 3-nm-thick CuI layer, J_{SC}, V_{OC} and *FF* have increased from 4.6±0.2 to 8.9±0.2 mA cm^{-2}, from 0.48±0.01 to 0.59±0.02 V, and from 0.56±0.01 to 0.61±0.02, respectively. As a result, the PCE result has increased 2.7 times from 1.2±0.1 to 3.2±0.1%.The increase in J_{SC} can be explained with the increase in the absorption of the ZnPc on CuI shown in Figure 4.2a. 20 nm-thick ZnPc on CuI shows about 1.6 times increase in absorption peak intensity at 628 nm than ZnPc on quartz with the same thickness.

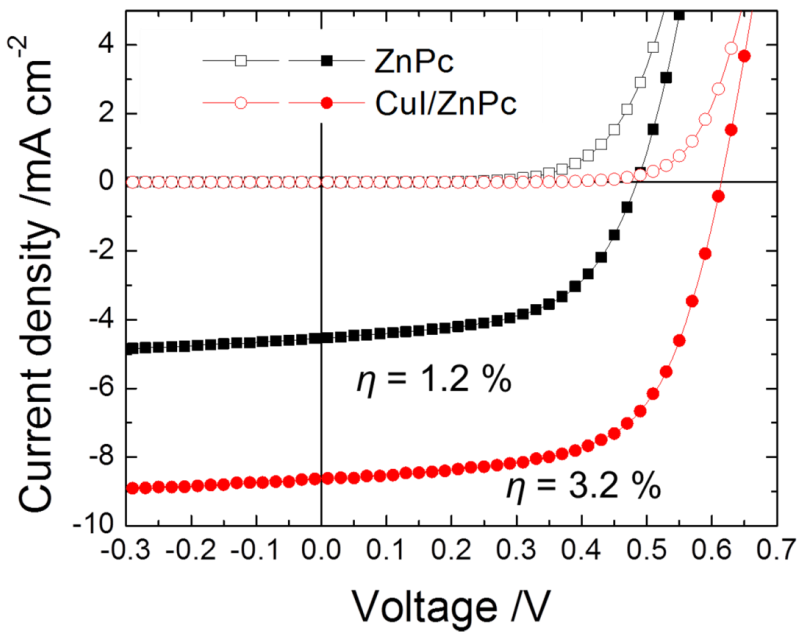

Figure 4.1 The current density-voltage characteristics of ITO/ZnPc 25 nm/C_{60} 40 nm/BCP 8 nm/Al 100 nm (black squares) and ITO/CuI 3 nm/ZnPc 25 nm/C_{60} 40 nm/BCP 8 nm/Al 100 nm (red circles) under dark (open symbols) and under AM1.5 solar simulator illumination (closed symbols).

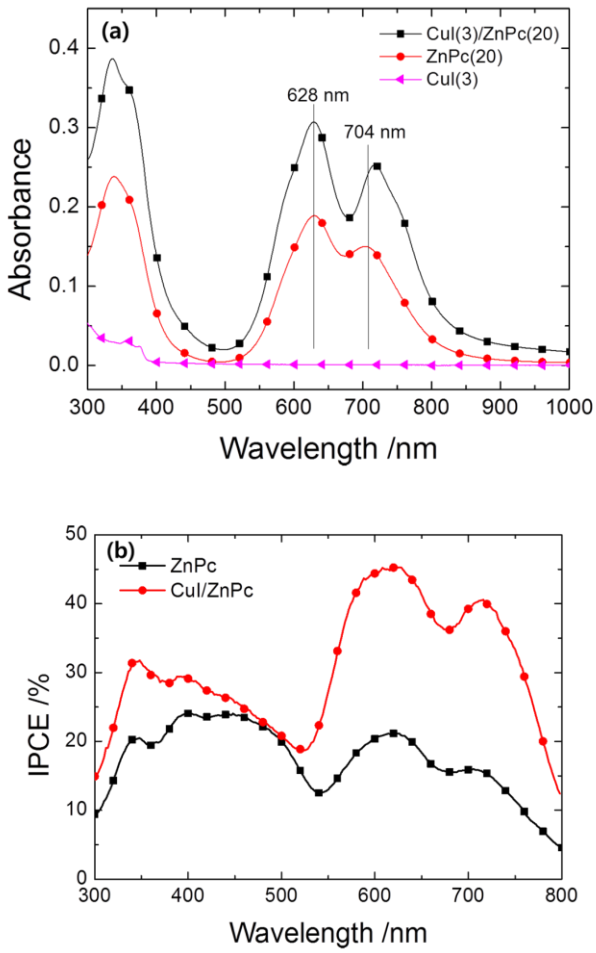

Figure 4.2(a) UV-VIS absorption spectra of CuI 3 nm, ZnPc 20 nm, and CuI 3 nm/ZnPc 20 nm on quartz substrates. 2 guide lines at 628 nm and 704 nm are drawn at the absorption peaks of ZnPc 20 nm. (b) IPCE spectra of ITO/ZnPc 25 nm/C_{60} 40 nm/BCP 8 nm/Al (black squares) and ITO/CuI 3 nm/ZnPc 25 nm/C_{60} 40 nm/BCP 8 nm/Al (red circles).

One can note that CuI does not contribute to the increased absorption, which is manifested by little absorption by CuI in the visible range. Since the transition dipole moment of ZnPc is located in the molecular plane [15], the enhanced absorption indicates that the ZnPc molecules are more preferentially oriented in the face-on direction on the CuI layer. Moreover, due to the strong bi-molecular interaction, the Q-band peak of 704 nm is red shifted to 720 nm [16]. This also helps to absorb more light with a broader range. The increased and broadened absorption has been reflected in the incident-photon-to electron conversion efficiency (IPCE) data shown in Figure 4.2b. The IPCE has increased up to 45% from 23% at the Q band due to the absorption enhancement. This increase in the IPCE in the Q-band is greater than that in absorption, implying that not only the enhanced absorption but also other factors such as the enhanced charge collection and exciton diffusion length by controlling the molecular orientation are contributing [17].The preferred face-on orientation of the ZnPc molecules on CuI was confirmed by wide angle x-ray scattering (WAXS) experiments. Figure 4.3 shows 2D WAXS images of ZnPc on Si (a) and on CuI 3nm/Si (b).

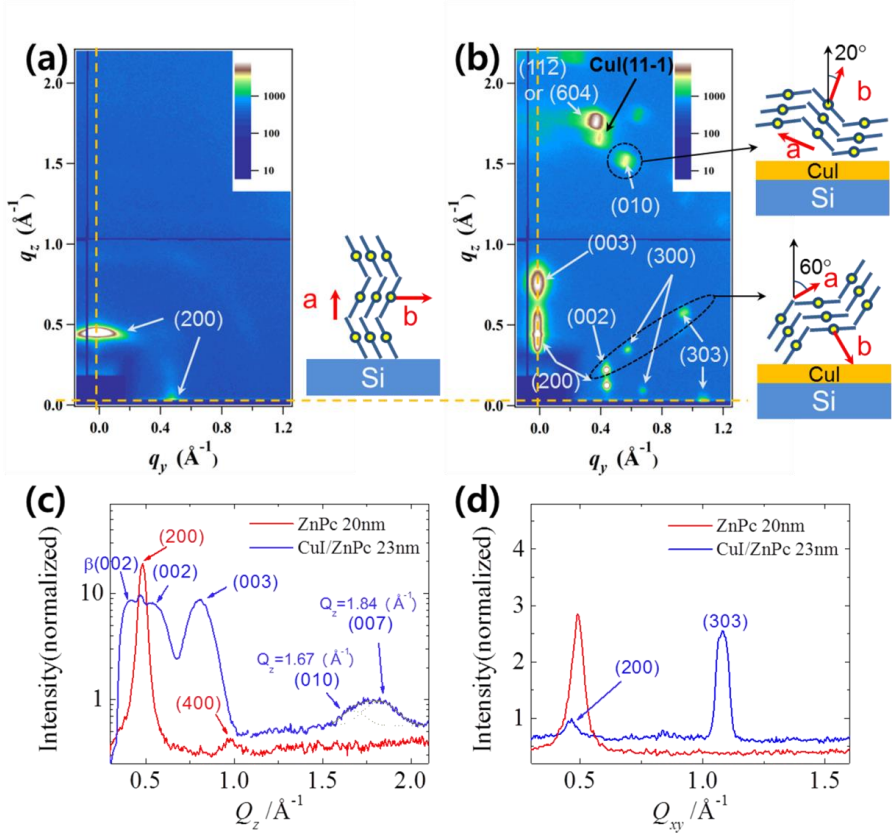

Figure 4.3 (a) and (b) are GIWAXS images of ZnPc on Si and CuI surfaces, respectively. (c) and (d) are vertical and horizontal line cut data of GIWAXS images as marked by dotted lines in (a) and (b). As shown in (c), the (010) peak relating to the lying configuration was observed in the vertical line cut data on the CuI surface. The (303) peak of the horizontal line cut data also supports the lying configuration of ZnPc molecules on the CuI surface. Dotted lines in (c) indicate peak fittings or (010) and (007).

Si wafers were treated with the piranha solution to have native oxide on the surface to have similar surface energy with the ITO [9].The axes of the ZnPc crystal are displayed in the inset of the figures. On the Si surface, ZnPc are stacked with the (200) preferred orientation as shown in Figure 4.3a. The strong (200) peak was measured in the vertical direction in the GIWAXS image manifesting the preferred edge-on orientation on the Si surface. A small and weak (200) peak was also observed in the horizontal plane, but the intensity is less than 15% of the vertically aligned (200) peak. On the other hand, the strong (003) peak and the (303) peak were measured on the CuI 3 nm/Si surface in the vertical and horizontal directions, respectively, in the GIWAXS image of Figure 4.3b, indicating that more ZnPc molecules are aligned with the face-on orientation. Molecular alignments contributing to the diffraction peaks are shown in the figures. Figure 4.3c and d show the vertical and horizontal line cuts of the GIWAXS images, respectively. In the vertical direction, the (200) peak intensity on CuI/Si decreased on CuI/Si decreased to the half on CuI/Si decreased to the half in comparison with the (200) peak intensity on Si, and the (003) intensity is comparable to the (200) intensity on CuI/Si (Figure 4.3c). In the horizontal direction, the (303) peak intensity on CuI/Si is as high as the (200) peak intensity on bare Si. Therefore, it seems that the number of face-on ZnPc molecules is similar to the number

of edge-on ZnPc molecules. The lattice parameters of the *a* and *c* axes are 2.6 nm and 2.38 nm, respectively. The lattice parameter of *b* is 0.376 nm [18]. The ZnPc molecules on CuI/Si show at least 3 kinds of preferred orientations with higher crystallinity than on Si. Compared to the (200) preferred aligned ZnPc on base Si, the mixed alignment of the face-on ZnPc and the (003) direction is more advantageous for absorbance of the light because the transition dipole moments of ZnPc are in the molecular plane.

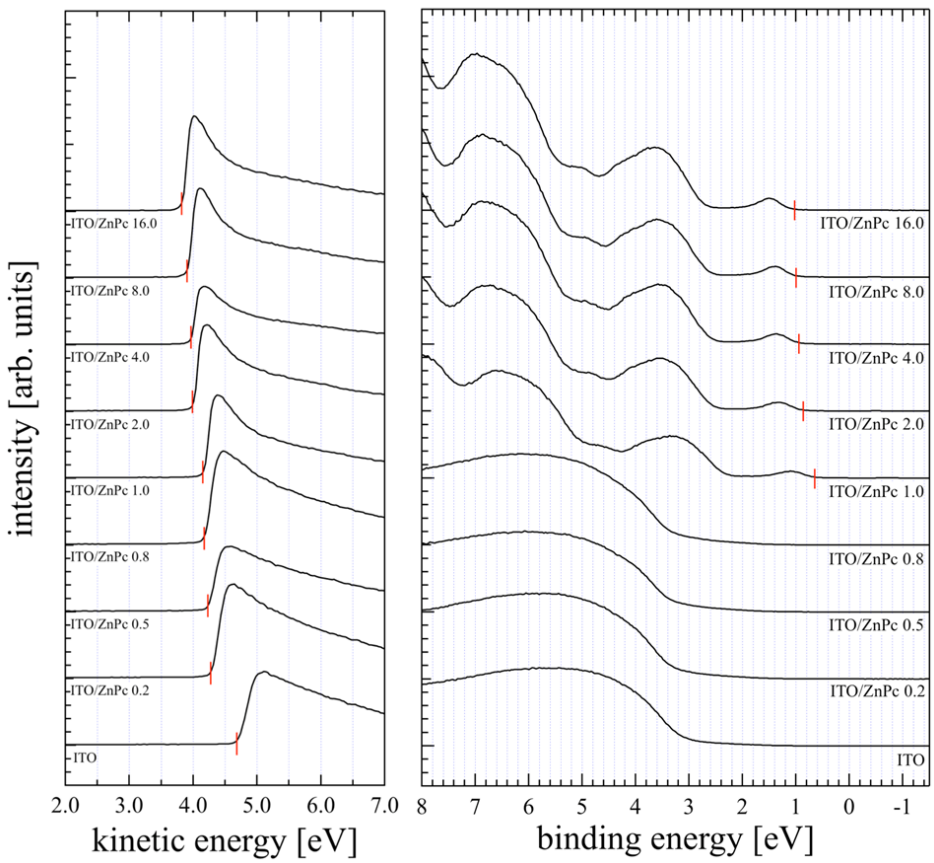

Figure 4.4 UPS spectra of ITO/ZnPc

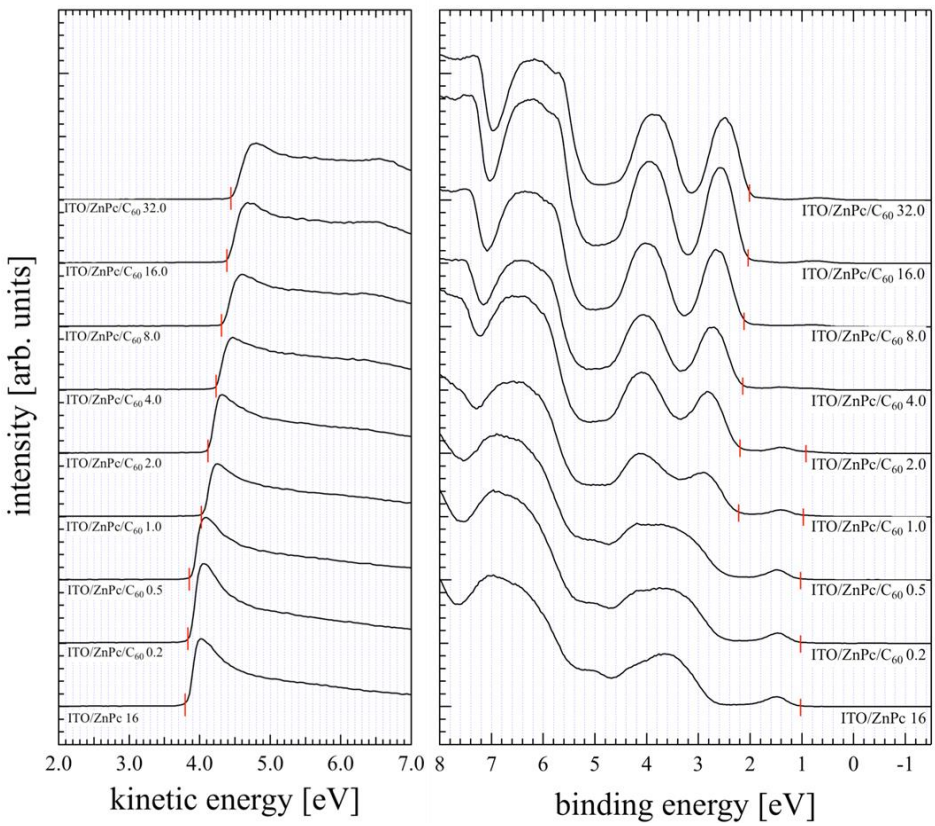

Figure 4.5 UPS spectra of ITO/ZnPc/C_{60}

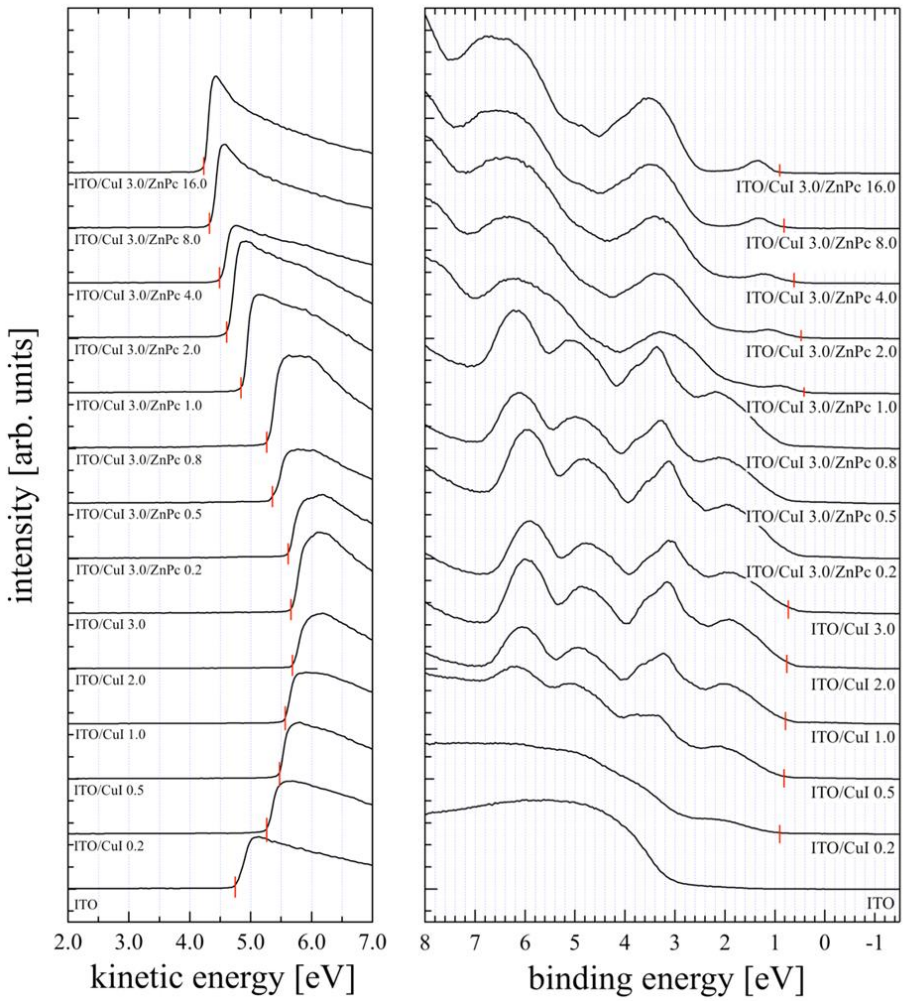

Figure 4.6 UPS spectra of ITO/CuI/ZnPc

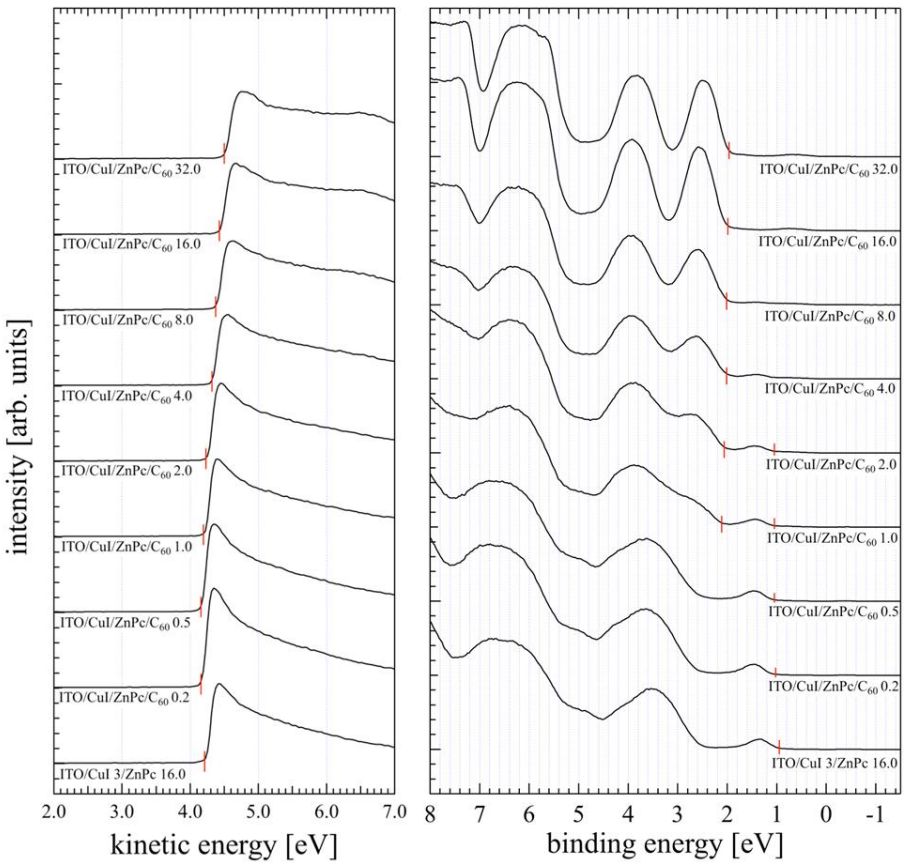

Figure 4.7 UPS spectra of ITO/CuI/ZnPc/C_{60}

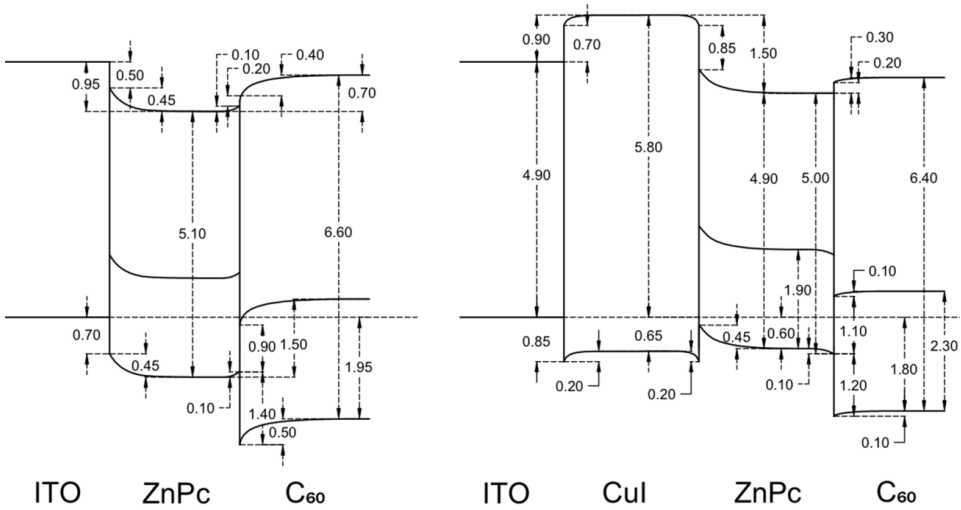

Figure 4.8 Energy band diagram of ITO/ZnPc/C_{60} and ITO/CuI/ZnPc/C_{60} extracted from the UPS measurement. (All numbers are in eV units)

Ultraviolet photoelectron spectroscopy (UPS) measurements were performed to investigate the increase of V_{OC} by mapping out the interfacial electronic structures. Figure 4.4, 4.5, 4.6, and 4.7 show the UPS spectra with the layers deposited. Figure 4.8 shows the energy diagrams of ITO/ZnPc/C_{60} and ITO/CuI/ZnPc/C_{60} constructed from the UPS data (Figure4.4-4.7). The vacuum levels (E_{VAC}) and HOMO levels were obtained from UPS, and the LUMO levels were determined by adding the reported transport band-gap of 1.90 and 2.30 eV for ZnPc [19] and C_{60}[20], respectively, to the HOMO levels. The HOMO levels were determined by the band edges, taking into account the effect of inhomogeneous broadening [21]. Due to the high work function of CuI (5.8 eV) strong interface dipoles are formed at both interfaces between ITO/CuI and CuI/ZnPc. Therefore, the difference between the HOMO level of the ZnPc donor and the LUMO level of the C_{60} acceptor at the interface increased from 0.90 to 1.10 eV as the CuI is inserted between the ITO and the ZnPc layer, which is closely related to the amount of the V_{OC} increase, as shown in Figure 4.1. The unusual downward band bending in ZnPc near the interface between ZnPc and C_{60} on CuI implies that the orientation of ZnPc at the ZnPc/C_{60} interface might change as C_{60} molecules are deposited on ZnPc due to the interaction with C_{60}. This bending seems to help exciton to dissociate easier. In addition, this

downward bending requires a higher bias for the device to be in the flat band condition, leading to the higher V_{OC}.

4.3.2 Introducing CuI to ATD bulk heterojunction OSCs

CuI have worked successfully to control ZnPc molecules to have face-on orientation. CuI layer is introduced to the bulk heterojunction OSCs using CuPc and C_{60} used in Chapter 2. With ATD, the more efficient charge transport route can be created. The molecular orientation control is applied to the ATD OSCs. For comparison codeposited OSCs are fabricated at the same time. 4 devices was fabricated as follow;ITO/ CuPc 3nm/CuPc:C_{60} codep 60 nm/C_{60} 10 nm/ BCP 8 nm/Al 100 nm, ITO/ CuPc 3nm/CuPc|C_{60} ATD 60 nm/C_{60} 10 nm/ BCP 8 nm/Al 100 nm, ITO/CuI 3 nm/CuPc 3nm/CuPc:C_{60} codep 60 nm/C_{60} 10 nm/ BCP 8 nm/Al 100 nm, and ITO/CuI 3 nm/CuPc 3nm/CuPc|C_{60} ATD 60 nm/C_{60} 10 nm/ BCP 8 nm/Al 100 nm. The mixing ratio for codeposited and ATD OSCs were 1:1, and the conditions for ATD were kept same as those of the ATD devices in Chapter 2. As shown in Figure 4.9, comparing two BHJ devices without CuI layer, ATD shows better performance than codeposited OSCs having advantage in J_{SC}. By introducing CuI layer as an orientation controlling layer, both codeposited and ATD OSCs show dramatic enhancement in V_{OC} and J_{SC}.

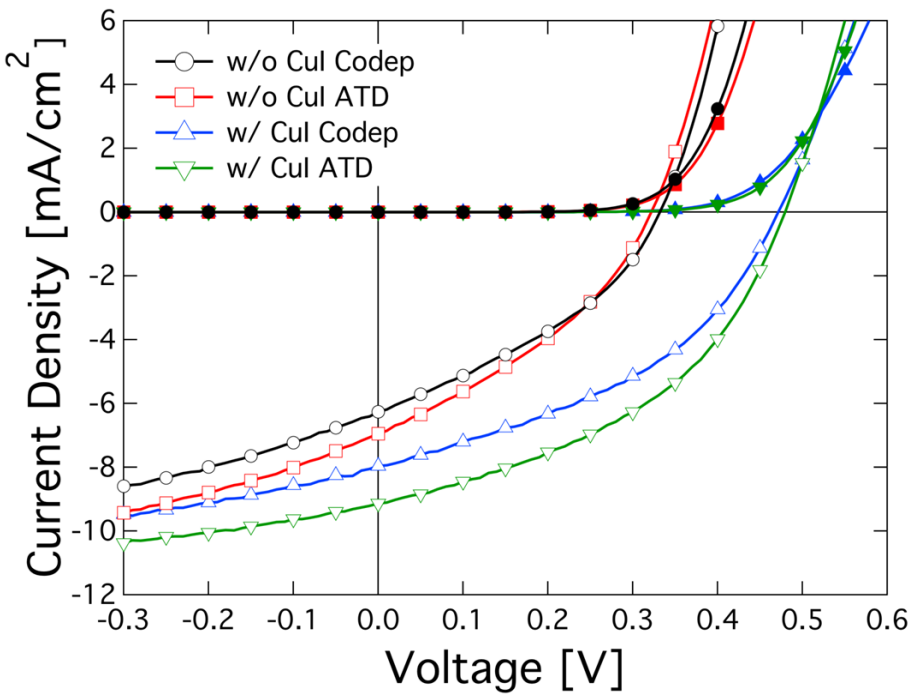

Figure 4.9 The current density-voltage characteristics of 4 devices: without CuI layer/codep. (black circles), without CuI layer/ATD (red squares), with CuI layer/codep. (blue triangles), and with CuI layer/ATD (green triangles) under dark (closed symbols) and under AM1.5 solar simulator illumination (open symbols).

Table 4.1 The power-conversion efficiency, PCE, short-circuit current, J_{SC}, open circuit voltage, V_{OC} and fill factor, *FF* of codeposited and ATD OSCs with or without CuI layer

	PCE [%]	*Jsc* [mA/cm^2]	*Voc* [V]	FF
w/ CuI ATD	1.90	9.14	0.48	0.43
w/o CuI ATD	0.793	6.95	0.32	0.36
w/ CuI Codep	1.56	7.96	0.47	0.42
w/o CuI Codep	0.749	6.26	0.33	0.36

In case of two OSCs with CuI layer, the ATD OSCs shows more improvement in J_{SC} compared to those without CuI layer, resulting 1.90% of PCE. This enhancement is mainly due to the increased amount of face-on CuPc molecules. The characteristics of OSCs are summarized in Table 4.1. Although further studies on the crystalline structures of codeposited and ATD BHJs on CuI are need, ATD seems to work better when the CuPc is laid down.

4.4 Conclusion

In conclusion, it is demonstrated that the control of molecular orientation is a very important method to improve the performance of organic solar. Using a CuI layer as the interfacial layer between the ITO and the thermally evaporated ZnPc layers, the proportion of the face-on molecules in the ZnPc layer on the CuI layer was significantly enhanced compared to the ZnPc layer without the CuI layer. These face-on ZnPc molecules can absorb more light due to the parallel alignment of their transition dipole moments to the polarization of the incident light, resulting in the increase in J_{SC}. In addition, the use of face-on ZnPc molecules helps to ensure a better charge transport path from the molecules in the vertical direction to ITO increasing the *FF*. The molecular orientation also affects their energy levels alignments to increase the V_{OC}. The resulting OSC showed a remarkably enhanced PCE of 3.2±0.1% compared to 1.2±0.1% for conventional OSCs which lack the control of molecular orientation. By introducing CuI to ATD OSCs, the overall performances of ATD OSCs were enhanced.

4.5 Bibliography

[1] S. Duhm, G. Heimel, I. Salzmann, H. Glowatzki, R. L. Johnson, A. Vollmer, J. P. Rabe, N. Koch, *Nat. Mater.*2008, **7**, 326-332.

[2] D. Yokoyama, Y. Setoguchi, A. Sakaguchi, M. Suzuki, C. Adachi, *Adv. Funct. Mater.*2010, **20**, 386.

[3] T. Matsushima, H. Murata, *Appl. Phys. Lett.*2011, **98**, 253307.

[4] M. F. Lo, T. W. Ng, T. Z. Liu, V. A. L. Roy, S. L. Lai, M. K. Fung, C. S. Lee, S. T. Lee, *Appl. Phys. Lett.*2010, **96**, 113303.

[5] B. P. Rand, D. P. Burk, S. R. Forrest, *Phys. Rev. B*2007, **75**, 115327.

[6] W. Chen, D.-C. Qi, H. Huang, X. Gao, A. T. S. Wee, *Adv. Funct. Mater.*2011, **21**, 410.

[7] H. Y. Mao, R. Wang, H. Huang, Y. Z. Wang, X. Y. Gao, S. N. Bao, A. T. S. Wee, W. Chen, *J. Appl. Phys.*2010, **108**, 053706.

[8] S. Braun, W. R. Salaneck, M. Fahlman, *Adv. Mater.*2009, **21**, 1450.

[9] H. J. Kim, J. W. Kim, H. H. Lee, T. M. Kim, J. Jang, J.-J. Kim, *J. Phys. Chem. Lett.*2011, **2**, 1710.

[10] L. Zhang, H. Peisert, I. Biswas, M. Knupfer, D. Batchelor, T. Chasse, *Surf. Sci.* 2005, **596**, 98.

[11] C. H. Cheng, J. Wang, G. T. Du, S. H. Shi, Z. J. Du, Z. Q. Fan, J. M. Bian, M. S. Wang, *Appl. Phys. Lett.*2010, **97**, 083305.

[12] H.-S. Shim, H. J. Kim, J. W. Kim, S.-Y. Kim, W.-I. Jeong, T.-M.

Kim, and J.-J. Kim, *J. Mater. Chem.* 2012,**22**, 9077.

[13] J. W. Kim, H. J. Kim, H. H. Lee, T. Kim, J.-J. Kim, *Adv. Funct. Mater.*2011, **21**, 2067.

[14] J. H. Lee, D. S. Leem, H. J. Kim, J.-J. Kim, *Appl. Phys. Lett.*2009, **94**, 123306.

[15] J. Mack, M. J. Stillman, *J. Phys. Chem.* 1995, **99**, 7935.

[16] J. S. Louis, D. Lehmann, M. Friedrich, D. R. T. Zahn, *J. Appl. Phys.*2007, **101**, 013503.

[17] R. R. Lunt, J. B. Benziger, S. R. Forrest, *Adv. Mater.*2010, **22**, 1233.

[18] N. Uyeda, M. Ashida, E. Suito, *J. Appl. Phys.*1965, **36**, 1453.

[19] W. Y. Gao, A. Kahn, *Org. Electron.*2002, **3**, 53.

[20] R. W. Lof, M. A. van Veenendaal, B. Koopmans, H. T. Jonkman, G. A. Sawatzky, *Phys. Rev. Lett.*1992, **68**, 3924.

[21] S. Krause, M. B. Casu, A. Scholl, E. Umbach, *New J. Phys.*2008, **10**, 085001.

Chapter 5.The crystalline structure of the interface between orientation controlled zinc phthalocyanine and copper iodide

5.1 Introduction

The molecular orientations in organic semiconductor devices play a great role to their performances. The out-coupling efficiencies can be enhanced by changing the dipole orientation of the emitter in organic light emitting diodes[1]. In organic thin film transistors, the crystallinity of the organic film and their preferred orientation are closely related to the performance of the organic devices[2]. Organic solar cells (OSCs) are also not an exception. The performance of an OSC is determined by three factors: the short circuit current (J_{SC}), open circuit voltage (V_{OC}), and fill factor (FF). All these factors are closely related to the molecular orientation that consist an OSC[3]. By matching the molecular transition dipole moment to the electric field of incident light, the total amount of absorption can be enhanced, increasing J_{SC}. The strength of their interface dipoles at organic-organic interfaces are also affected by the molecular orientation, resulting in the change of V_{OC}[4]. Disk-shape molecules such as metal phthalocyanines grow with edge-on orientations when thermally deposited on indium tin oxide (ITO)[5,6]which is not favorable for light

absorption and charge transport. When introducing copper iodide (CuI) layer the crystalline structure can be modified to have face-on orientation for copper phthalocyanine (CuPc)[7], zinc phthalocyanine (ZnPc)[8], and lead phthalocyanine (PbPc)[9]. For ZnPc, we have previously reported 2.7 times enhancement in power conversion efficiency (PCE) by introducing the CuI layer to ZnPc showing 3.2±0.1% with a planar heterojunction solar cell in Chapter 4.

In spite of the enhancement in performance, the mechanism of formation of face-on orientation is not clear. Understanding the mechanism will able to find this interfacial layer for other materials. Hereby we studied on the crystalline structure of ZnPc close to the CuI interface and that of ZnPc far from the interface, and propose the mechanism of formation of face-on orientations. Glazing incidence wide angle x-ray scattering (GIWAXS) was used to distinguish the different crystalline structures of ZnPc at two regions.

5.2 Experiments

GIWAXS measurements were performed at 12IDB and 12IDC beamline of the Advanced Photon Source (APS). The x-ray energy was 12 keV, and distance from the sample to detector was 227 mm. A 2D CCD detector PILATUS 2M was used. GIWAXS were measured at the incidence angle of 0.05 and 0.20, which are smaller and higher than the critical angle, 0.124, calculated with a mass density of 1.62 g cm^{-3} for the monoclinic gamma ZnPc structure[6]. The samples for GIWAXS measurement were prepared on a silicon wafer treated with piranha solution (H_2SO_4:H_2O_2 = 4:1) treated silicon wafer. ZnPc and CuI were purchased from Aldrich and ZnPc was purified twice by sublimation before deposition. 3-nm-thick CuI and 20-nm-thick ZnPc layers were successively deposited by thermal evaporation under a vacuum of 10^{-7} torr.

5.3 Results and discussions

Figure 5.1 shows the crystalline structures of β and γ phase of ZnPc and gamma phase CuI used for GIWAXS analysis. The unit cell parameters of the monoclinic C2/n γ-ZnPc were a = 2.60 nm, b = 0.376 nm, and$c$ = 2.38 nm, with β = 94.2845°[10]. That of the monoclinic $P2_1/c$ β-ZnPc were a = 1.93 nm, b = 0.485 nm, and c = 1.46 nm, with β = 120.48°[11]. CuI had the F23m structure with a= 0.6063 nm[12]. VESTA software was used for crystal visualization[13] Based on these crystal parameters, GIWAXS data have analyzed.

In order to distinguish the ZnPc crystalline structures in the surface region from the CuI/ZnPc interface region, GIWAXS were measured at the incidence angle of 0.05° and 0.20°, which are smaller and higher than the critical angle, 0.124°, calculated with a mass density of 1.62 g cm^{-3} for the monoclinic gamma ZnPc structure[6]. As describe in Figure 5.2a, with the incidence angle of 0.05° (below the critical angle), the penetration depth of x-ray is only 4 nm. Therefore GIWAXS image is mainly from the crystal structure of ZnPc within only few nanometers from the surface. On the other hand, with the incidence angle of 0.20° (above the critical angle), x-ray penetrates all through the films including the CuI layer and ZnPc at the CuI/ZnPc interface.

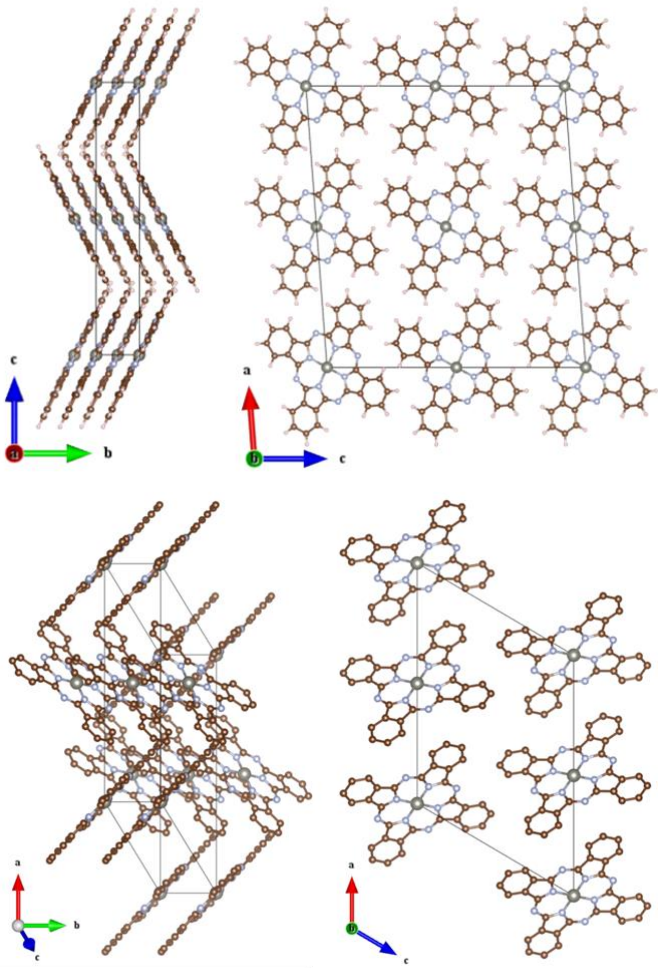

Figure 5.1 The unit cell parameters of βphase and γphase ZnPc used to index the peaks.

Figure 5.2b and c shows the GIWAXS images taken with the incidence angles of 0.05° and 0.20°, respectively. As diffraction peaks are coming from the ZnPc near the surface with the incidence angle of 0.05 most peaks in Figure 5.2b and c are coming from the ZnPc. Strong (200) peak and the (303) peak were observed in the vertical and horizontal directions, respectively, indicating that ZnPc molecules are aligned with the face-on orientation. In addition, (00l) peaks at high *Qz* region are not able to be observed in GIWAXS because as *Qz* increases the deviation from theta-2theta condition where the *Qz* scattering vector is surface normal increases in GIWAXS measurement, theta-2theta scan at the high *Q* region were performed. ZnPc on CuI layer has the preferred orientation of (313) in gamma phase as shown in Figure 5.3. This is correlated with the (300) and (002) diffraction, which create plane angle of 67° and 65° with (313) respectively. Different diffraction peaks with the incidence angles are resulted from CuI layer and the different crystalline structure of ZnPc at the interface. The vertically elongated CuI peaks in Figure 5.2c imply that the CuI has formed uniform thin layer with the orientation of (111). The other differences in the diffraction are observed along the *Qz* direction.

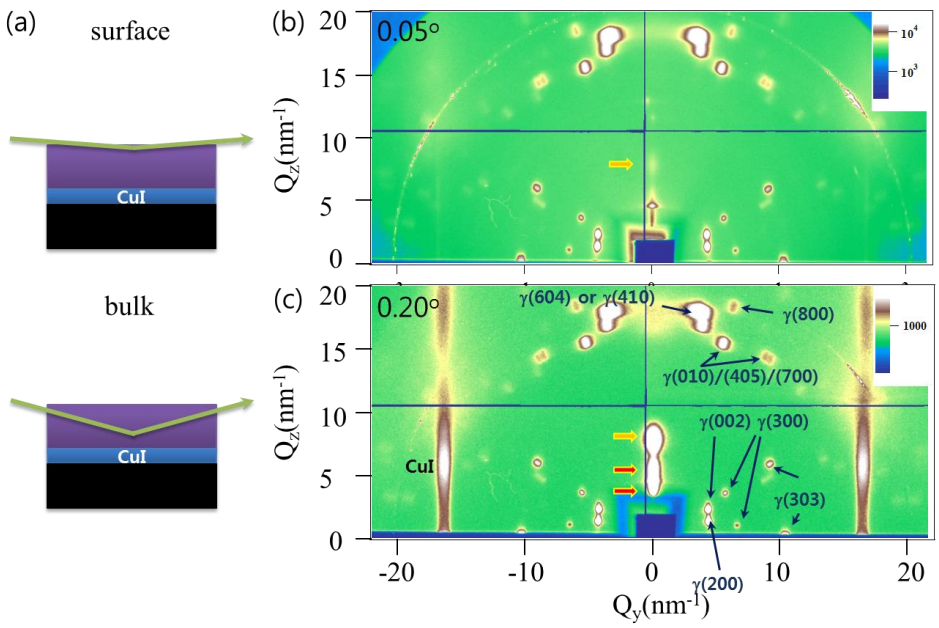

Figure 5.2 GIWAXS images of two different incidence angles; 0.05° and 0.20°. 0.20° data shows the bulk property of the film and 0.05° data shows the property of the surface of the film (ZnPc 20 nm/CuI 3 nm/Si) due to the penetration depth difference with the incident angle. In the bulk film, ZnPc beta phase appears, which is not observed in the surface of the film, indicating that beta phase exist close to CuI layer.

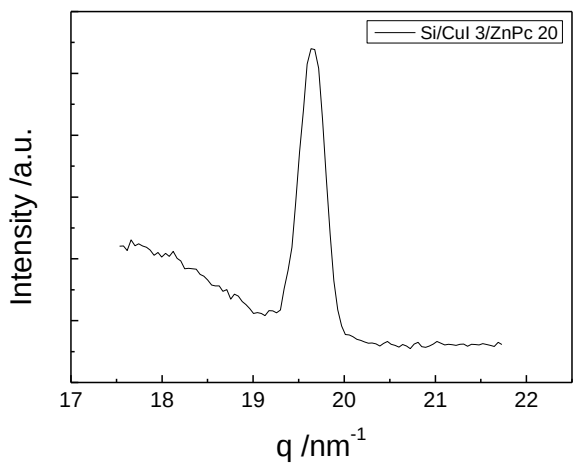

Figure 5.3 XRD of Si/CuI (3 nm)/ZnPc (20 nm) at the high q region

To analyze the difference, vertical line cut along the *Qz* direction is performed as shown in Figure 5.4. For 0.05°, gamma (200) and gamma (003) are the only peaks observed. For 0.20°, to identify the peaks, 6 Gaussian functions were used to fit the curve, which showed the best fitting results. Red circle indicates the data and red line is the fitting results for each peaks. β(100) and strong $\beta(\bar{1}01)$ were found which is not observed in the surface of the ZnPc film, indicating that the β phasecrystal with preferred orientation of $(\bar{1}01)$exist close to CuI layer. γ phase of ZnPc are kept observed strongly due to the increase of penetration depth.

The existence of ZnPc beta phase seems to play a great role to orientate the ZnPc molecules face-on. As described in Figure 5.5, lattice points of the crystals are drawn due to the simplicity with the lattice parameters shown in Figure 5.1. When we draw the lattice points of ZnPc β $(\bar{1}01)$ over that of CuI (111), lattice points are very well matched each other inferring epitaxy-like growth [14]regarding the variation of lattice parameters in organic materials. In addition ZnPc γ(313) also matches ZnPc $(\bar{1}01)$ with larger super lattice. Although ZnPc $\beta(\bar{1}01)$ has edge-on orientation ZnPc molecules are more tilted than γ ZnPc, it seems to work as a buffer layer to induce γ ZnPc to have face-on orientation to have energetically favorable.

Proposed mechanism of inducing face-on orientation of ZnPc is described in Figure 5.5. When ZnPc layer is thermally deposited on CuI layer, thin β phase ZnPc with $(\bar{1}01)$ direction forms on the (111) CuI layer. Then (313) γ ZnPc sits on the β ZnPc layer. These transitions can be explained with quasi epitaxial growth.

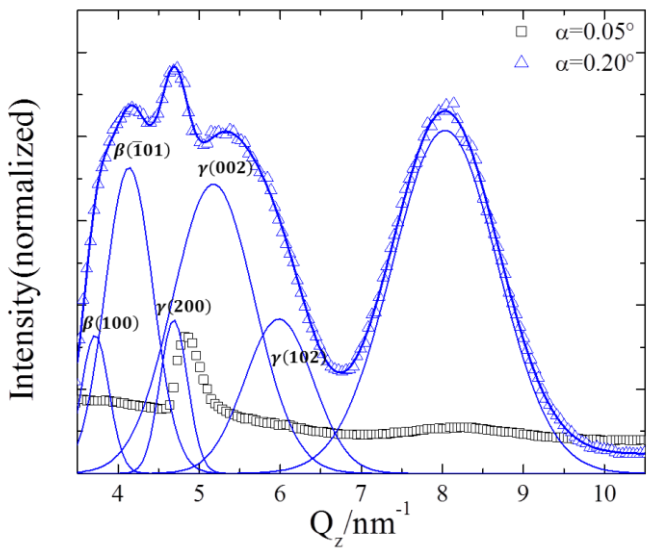

Figure 5.4 Line cut of GIWAXS image shown in Figure 5.2 in Q_z direction for incidence angle of 0.05 (black squares) and 0.20 (blue triangles). Blue lines indicate peak fitting with Gaussian functions based on their crystal structures.

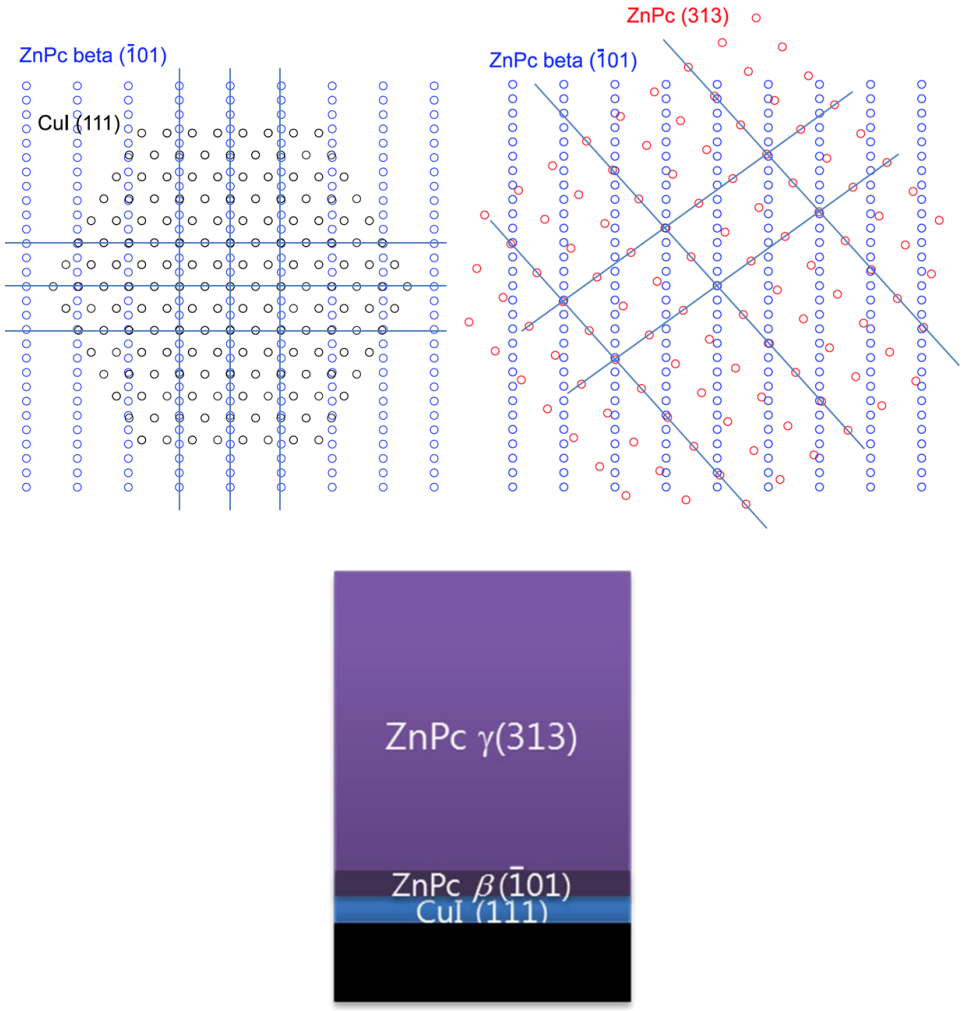

Figure 5.5 Proposed layer structure and its mechanism. When ZnPc layer is thermally deposited on CuI layer, thin beta phase ZnPc with ($\bar{1}$01) direction forms on the (111) CuI layer. Then (313) gamma ZnPc sits on the beta ZnPc layer. Quasi organic epitaxial growth showing the super lattice as drawn above.

5.4 Conclusion

The crystalline structure of Si/CuI (3 nm)/ZnPc (20 nm) film is investigated using different incidence angle using GIWAXS. By using 0.05 and 0.20 which are smaller and greater the critical angle, the penetration depth of x-ray in the sample could be controlled. This allows us to distinguish the crystal structure of ZnPc close to CuI/ZnPc interface and ZnPc at the surface. We have found the existence of the beta phase of ZnPc with the preferred orientation of $(\bar{1}01)$, which was not observed in the ZnPc near the surface. The $(\bar{1}01)$ plane lattice points were well matched with (111) CuI, inferring the epitaxial growth in organic materials. This beta phase also induces to ZnPc to have gamma phase with preferred orientation of (313), face-on orientations, which is favorable for OSC application.

5.5 Bibliography

[1] S.-Y. Kim, W.-I.Jeong, C. Mayr, Y.-S.Park, K. H. Kim, J.-H.Lee, C.-K.Moon, W. Brütting, J.-J. Kim, *Adv. Funct. Mater.***2013**, DOI 10.1002/adfm.201300104.

[2]T. Matsushima, H. Murata, *Appl. Phys. Lett.***2011**, *98*, 253307.

[3] B. P. Rand, D. Cheyns, K. Vasseur, N. C. Giebink, S. Mothy, Y. Yi, V. Corpceanu, D. Beljonne, J. Cornil, J.-L. Brédas, J. Genoe, *Adv. Funct. Mater.***2012**, *22*, 2987–2995.

[4] W. Chen, D.-C. Qi, H. Huang, X. Gao, A. T. S. Wee, *Adv.Funct.Mater.***2010**, *21*, 410–424.

[5] H. J. Kim, J. W. Kim, H. H. Lee, T.-M. Kim, J. Jang, J.-J. Kim, *J. Phys. Chem. Lett.***2011**, 1710–1714.

[6] H. J. Kim, J. W. Kim, H. H. Lee, B. Lee, J.-J. Kim, *Adv.Funct.Mater.***2012**, *22*, 4244–4248.

[7] C. H. Cheng, J. Wang, G. T. Du, S. H. Shi, Z. J. Du, Z. Q. Fan, J. M. Bian, M. S. Wang, *Appl. Phys. Lett.***2010**, *97*, 083305–083305–3.

[8] J. W. Kim, H. J. Kim, T.-M. Kim, T. G. Kim, J.-H.Lee, J. W. Kim, J.-J. Kim, *Curr. Appl. Phys.***2012**, *13*, 7–11.

[9] H. J. Kim, H.-S. Shim, J. W. Kim, H. H. Lee, J.-J. Kim, *Appl. Phys. Lett.***2012**, *100*, 263303.

[10] M. Ashida, N. UYEDA, E. SUITO, *B Chem Soc Jpn***1966**, *39*,

2616.

[11] W. R. Scheidt, W. Dow, **1977**, *99*, 1101–1104.

[12] S. Hull, D. Keen, W. Hayes, N. Gardner, *J Phys-Condens Mat***1998**, *10*, 10941–10954.

[13] K. Momma, F. Izumi, *Journal of Applied Crystallography***2011**, *44*, 1272–1276.

[14] S. Forrest, *Chem Rev***1997**, *97*, 1793–1896.

국문초록

급증하는 에너지 소비추세와 지구온난화와 같은 환경오염에 대한 우려로 태양에너지는 화석연료를 대체하는 에너지원으로 각광받고 있다. 그 중 유기태양전지는 다른 태양전지와 비교하여 낮은 전력변환효율을 현시점에서는 보이고 있지만 유기재료들의 값이 싸고 대면적으로 제작하는 비용이 적게 들고 용이하기 때문에 유기태양전지 효율향상을 위한 연구가 집중되고 있다. 본 연구를 통해 단분자 유기재료를 이용하여 효율적인 유기태양전지를 분자배향과 나노구조의 제어를 통해서 구현하였다.

유기태양전지에 유리한 상분리 구조 형성이 용이한 고분자 재료와는 달리 저분자에서는 높은 자유도로 인하여 상분리가 어렵다. 이를 해결하기 위해 교차증착이라는 새로운 방법을 제시하여 저분자에서 구현하기 어려운 유기태양전지에 보다 적합한 혼합층을 형성하였고 이 교차증착법으로 제작한 CuPc 와 C_{60} 를 사용한 유기태양전지에서 기존 공증착법보다 높은 효율을 보였다. 이 방법으로 형성한 혼합층을 UV-VIS 흡수와 x-선 실험을 통해 혼합층이 공증착보다 aggregation 이 형성되고 디스크 형태의 구조를 갖춘 것을 확인하였다. CuPc 와 동일한

결정구조를 지닌 ZnPc 의 경우 교차증착법으로 인한 효율증가가 보이지 않았지만 초기 막성장양태가 디스크형태를 이루는 CuPc 와는 달리 ZnPc 의 경우 초기 성장시에 특별한 구조가 없음을 확인하여 교차증착법으로 유기태양전지에 유리한 혼합층을 만들기 위해서는 초기 성장의 중요함을 알았다. 초기성장의 양태에 변화를 주는 한 요인으로 표면에너지에 따른 CuPc 의 초기 성장 구조를 x-선 분석을 통해 보았다. 친수성표면위에서는 배수성 표면위보다 더 큰 결정구조와 나노입자 구조를 보이는 것을 확인하였다. 친수성 표면 위에서 CuPc 결정입자가 더 규칙적으로 존재하지만 결정입자들 사이의 간격이 존재함을 확인하였고 이로 인해 유기박막트랜지스터에서는 더 낮은 전하 이동도를 보였으며 표면에너지의 제어로 막성장 양태에 변화를 줄 수 있음을 알 수 있었다. 보다 높은 전력변환효율을 얻기 위해 분자배향층을 유기태양전지에 적용하였다. 분자배향을 제어하게 되면 개방전압, 단락전류, 전도도 등을 제어 할 수 있어 유기 태양전지에 유리하다. CuI 분자배향층을 이용하여 ZnPc 분자의 빛의 흡수에 유리한 수평배향의 양을 증대시켜 동일한 물질을 사용면서도 2 배 이상의 고효율의 유기태양전지를 제작하였다. x-선으로 분자배향층과

ZnPc 계면에 $(\bar{1}01)$ 우선배향을 가지는 베타상이 존재하며 이 베타상이 ZnPc 의 (313)방향의 수평배향을 유도 하는 Epitaxy 와 유사한 기작을 제시하였다.

키워드: 유기태양전지, 혼합층, 분자배향, 결정구조

학번: 2007-30178

CURRICULUM VITAE

Personal Information

Name:	Ji Whan Kim
Date of Birth:	December 2, 1977
Nationality:	Republic of Korea
Present address:	Rm# 120, BLDG#39, Seoul National University, 1 Gwanak-ro, Gwanak-gu, Seoul, Korea
Phone numbers:	+82-2-875-2412 (office), +82-2-889-8702 (fax), +82-10-2718-7677 (mobile)
Email:	suchem57@snu.ac.kr

Education

2007.3~2013.8	Ph. D. Department of Materials Science and Engineering, Seoul National University, Seoul, Korea (Supervisor: Prof. Jang-Joo Kim) Thesis: "Efficient small-molecular-weightorganic solar cells through orientation control and nano-structuring"

2004.3~2006.2	Master of Engineering Department of Materials Science and Engineering, Seoul National University, Seoul, Korea (Supervisor: Prof Jang-Joo Kim) Thesis: “Improvement of electroluminescent efficiency using a novel host in blue phosphorescent organic light emitting diodes”
1996.3~2004.2	Bachelor of Science Department of Chemical and Biological Engineering, Seoul National University, Seoul, Korea

Experiences

2007.3~2007.8	Teaching assistant
2006.3~2007.2	Worked as a researcher at Center for Organic light emitting diodes, Seoul National University, Seoul, Korea.
2004.3~2004.8	Teaching assistant
2000.3~2002.5	Military services as Korean Augmentation To the United States Army (KATUSA), Attended the Primary Leadership Development Course (PLDC)

Professional Activities

A. Membership:

- Member of Society for Information Display
- Member of the Polymer Society of Korea
- Member of Korea Synchrotron Radiation User's Association

Research Interests

Organic Photovoltaic, Organic light emitting diodes, Organic Semiconductor laser, Organic electronics, Photo-physics of organic materials, nanostructure analysis of bulk heterojunction using x-ray

Professional Skills

A. Instrumental handled:

Organic electronic device fabrication, device characteristic measurement, UV-visible-NIR absorption spectrophotometer, Transient photo-luminescence and electro-luminescence measurements, x-ray reflectivity measurement (XRR), x-ray diffraction measurement (XRD), small or wide angle x-ray scattering (SAXS, WAXS), Time of flight (TOF) measurement, Atomic Force Microscopy (AFM), Ultraviolet photo-electron spectroscopy (UPS), x-ray photoelectron spectroscopy (XPS),

Scanning electron microscope (SEM), Transmission Electron Microscopy (TEM)

B. Computational skills:

MATLAB, LabView

Scholarship and Fellowship

2007.9~2011.2 Brain Korea 21 Scholarship

Award

1. "Outstanding Paper Award for Graduate students," Korea Synchrotron Radiation User's Association, Nov. 17, 2011
2. Ji Whan Kim, Hyo Jung Kim, Tae-Min Kim, Tae Gun Kim, Jeong-Hwan Lee, Jeong Won Kim and Jang-Joo Kim, "Best Poster Award," The 3rd Asian Conference on Organic Electronics, Nov. 4-6, 2011
3. Tae-Min Kim, Ji Whan Kim, Hyun Sub Shim and Jang-Joo Kim, "Best Poster Award", The 3rd Asian Conference on Organic Electronics, Nov. 4-6, 2011
4. The Army Commendation Medal, Apr. 23, 2002, Permanent orders #113-1
5. The Army Achievement Medal, May 14, 2001, Permanent orders

#134-4

6. The Army Achievement Medal, Jan. 20, 2001, Permanent orders #20-8

List of Publications

1. Hyun-Sub Shim, Sei-Yong Kim, Ji Whan Kim, Tae-Min Kim, Chang-Heon Lee, Jang-Joo Kim, “An efficient interconnection unit composed of electron-transporting layer/metal/p-doped hole-transporting layer for tandem organic photovoltaics.” ***Appl. Phys. Lett.***, 102, 203903 (2013)

2. Hyo Jung Kim, Jeong-Hwan Lee, Ji Whan Kim, Sunghun Lee, Junhyuk Jang, Hyun Hwi Lee and Jang-Joo Kim, “Molecular alignment and nanostructure of 1,4,5,8,9,11-hexaazatri-phenylene-hexanitrile (HATCN) thin films on organic surfaces.” ***J. of Mater. Chem. C***, 1, 1260 (2013)

3. Tae-Min Kim,[†]Ji Whan Kim,[†] Hyun-Sub Shim, Jang-Joo Kim, “High efficiency and high photo-stability zinc-phthalocyanice based planar heterojunction solar cells with a double interfacial layer,” ***Appl. Phys. Lett.***, 101, 113301 (2012)

   [†] These authors contributed equally to this work.

4. Hyo Jung Kim, Hyun-Sub Shim, Ji Whan Kim, Hyun Hwi Lee, Jang-Joo Kim, "CuI interlayers in lead phthalocyanine thin films enhance near-infrared light absorption," ***Appl. Phys. Lett.***, 100, 263303 (2012)

5. Ji Whan Kim, Hyo Jung Kim, Tae-Min Kim, Tae Gun Kim, Jeong-Hwan Lee, Leong Won Kim, Jang-Joo Kim, "High Performance Organic Planar Heterojunction Solar Cells by Controlling the Molecular Orientation," ***Curr. Appl. Phys***., 13, 7 (2013)

6. Hyo Jung Kim, Ji Whan Kim, Hyun Hwi Lee, Byeongdu Lee, and Jang-Joo Kim, "Initial growth mode, nanostructure and molecular stacking of a ZnPc:C_{60} bulk heterojunction," ***Adv. Funct. Mater.***, 22, 4244 (2012)

7. Hyo Jung Kim, Hyun Hwi Lee, Ji Whan Kim, Junhyuk Jang, Jang-Joo Kim, "Surface dependent thermal evolution of the nanostructures in ultra-thin copper(II) phthalocyanine films," ***J. of Mater. Chem.***, 22, 8881 (2012)

8. Hyun-Sub Shim, Hyo Jung Kim, Ji Whan Kim, Sei-Yong Kim, Won-Ik Jeong, Tae-Min Kim, and Jang-Joo Kim, "Enhancement of near-infrared absorption with high fill factor in lead phthalocyanine-based organic solar cells," ***J. of Mater. Chem.***, 22, 9077 (2012)

9. Jeong-Hwan Lee, Ji Whan Kim, Sei-Yong Kim, Seung-Jun Yoo, Jae-Hyun Lee, and Jang-Joo Kim, "An organic p-n junction as an efficient and cathode independent electron injection layer for flexible inverted organic light emitting diodes," ***Org. Electron.***, 13, 545-549 (2012)

10. Hyo Jung Kim, Ji Whan Kim, Hyun Hwi Lee, Tae-Min Kim, Junhyuk Jang, and Jang-Joo Kim, "Grazing Incidence Small-Angle X-ray Scattering Analysis of Initial Growth of Planar Organic Molecules Affected by Substrate Surface Energy," ***J. of Phys. Chem. Lett.***, 2, 1710 (2011)

11. Hyo Jung Kim, Ji Whan Kim, Jang-Joo Kim, "Invited Paper: Nanostructures of a mixed donor and acceptor layer in organic photovoltaics," ***Electronic Materials Letters***, 7, 93 (2011)

12. Ji Whan Kim,† Hyo Jung Kim,† Hyun Hwi Lee, Taemin Kim, Jang-Joo Kim, "Formation of bulk heterojunctions by alternative thermal deposition and its structure analysis for high efficiency small molecular organic photovoltaics," ***Adv. Funct. Mater.***, 21, 2067 (2011)

    † These authors contributed equally to this work.

13. Dong-Seok Leem, Sungsoo Kim, Ji Whan Kim, Jung Inn Sohn, Angharad Edwards, Jingsong Huang, Xuhua Wang, Jang-Joo Kim, Donal D. C. Bradley, and John C. deMello, "Rapid Patterning of Single-Wall Carbon Nanotubes by Interlayer Lithography," ***Small***, 6, 2530 (2010)

14. Dong-Seok Leem, Ji Whan Kim, Sung Ouk Jung, Seul-Ong Kim, Se Hoon Kim, Kee Young Kim, Yun-Hi Kim, Soon-Ki Kwon, and Jang-

Joo Kim, "Efficient and colour-stable hybrid white organic light-emitting diodes utilizing electron–hole balanced spacers," ***J. Phys. D: Appl. Phys.,*** 43, 405102 (2010)

15. Ying Zhou,[†] Ji Whan Kim,[†] Raju Nandhakumar, Min Jung Kim, Eunae Cho, Youn Soo Kim, Yoon Hee Jang, Chongmok Lee, Seungwu Han, Kwan Mook Kim, Jang-Joo Kim and Juyoung Yoon, "Novel binaphthyl-containing bi-nuclear boron complex with low concentration quenching effect for efficient organic light-emitting diodes," ***Chem. Comm.***, 46, 6512 (2010)

    [†] These authors contributed equally to this work.

16. Ying Zhou,[†] Ji Whan Kim,[†] Min Jung Kim, Won-Joon Son, Su Jung Han, Ha Na Kim, Seungwu Han, Youngmee Kim, Chongmok Lee, Sung-Jin Kim, Dong Ha Kim, Jang-Joo Kim, and Juyoung Yoon, "Novel Bi-Nuclear Boron Complex with Pyrene Ligand: Red-Light Emitting as well as Electron Transporting Material in Organic Light-Emitting Diodes," ***Org. Lett.***, 12, 1272 (2010)

    [†] These authors contributed equally to this work.

This article has been highlighted by "Noteworthy Chemistry, ACS" on April 19, 2010

http://portal.acs.org/portal/acs/corg/content?_nfpb=true&_pageLabel=PP_ARTICLE

MAIN&node_id=840&content_id=CNBP_024654&use_sec=true&sec_url_var=region1&__uuid=c458e897-5d43-45dd-80f1-0e1689ed203f

17. Dong-Seok Leem, Sung Ouk Jung, Seul-Ong Kim, Jong-Won Park, Ji Whan Kim, Young-Seo Park, Yun-Hi Kim, Soon-Ki Kwon, and Jang-Joo Kim, "Highly efficient orange organic light-emitting diodes using a novel iridium complex with imide group-containing ligands," ***J. Mater. Chem.***, 19,8828 (2009)

18. Jong Won Chung, Byeong-Kwan An, Ji Whan Kim, Jang-Joo Kim and Soo Young Park, "Self-assembled perpendicular growth of organic nanoneedles via simple vapor-phase deposition: one-step fabrication of a superhydrophobic surface," ***Chem. Commun.***, 2008, 2998 (2008)

19. Jae-Wook Kang, Deug-Sang Lee, Hyung-Dol Park, Ji Whan Kim, Won-Ik Jeong, Young-Seo Park, Se-Hyung Lee, Kyungmoon Go, Jong-Soon Lee, Jang-Joo Kim, "A host material containing tetraphenylsilane for phosphorescent OLEDs with high efficiency and operational stability," ***Organic Electronics*** 9, 452 (2008)

20. Nam Su Kang, Byeong-Kwon Ju, Ji Whan Kim, Jang-Joo Kim, Jae-Woong Yu, and Byung Doo Chin, "Correlation of photoluminescent quantum efficiency and device characteristics for the soluble

electrophosphorescent light emitter with interfacial layers," ***J. Appl. Phys.***, 104, 024511 (2008)

21. Junhyuk Jang, Ji Whan Kim, Nohhwal Park, and Jang-Joo Kim, "Air stable C_{60} based n-type organic field effect transistor using a perfluoropolymer insulator," ***Organic Electronics*** 9, 481 (2008)

22. Joo Hyun Kim, Do Yeung Yoon, Ji Whan Kim, and Jang-Joo Kim, "New host materials with high triplet energy level for blue-emitting electrophosphorescent device," ***Synthetic Metals*** 157, 743 (2007)

23. Jae-Wook Kang, Deug-Sang Lee, Hyung-Dol Park, Young-Seo Park, Ji Whan Kim, Won-Ik Jeong, Kyung-Mo Yoo, Kyoungmoon Go, Se-Hoon Kim and Jang-Joo Kim, "Silane- and triazine-containing hole and exciton blocking material for high-efficiency phosphorescent organic light emitting diodes," ***J. Mater. Chem.***, 17, 3714 (2007)

24. Dong-Seok Leem, Hyung-Dol Park, Jae-Wook Kang, Jae-Hyun Lee, Ji Whan Kim, and Jang-Joo Kim, "Low driving voltage and high stability organic light-emitting diodes with rhenium oxide-doped hole transporting layer," ***Appl. Phys. Lett.***, 91, 011113 (2007)

25. Tae-Hyuk Kwon, Hyo Soon Cho, Myoung Ki Kim, Ji-Whan Kim, Jang-Joo Kim, Kwan Hee Lee, Su Jin Park, Ik-Soo Shin, Hasuck Kim, Dong Mok Shin, Young Keun Chung, and Jong-In Hong, "Color

Tuning of Cyclometalated Iridium Complexes through Modification of Phenylpyrazole Derivatives and Ancillary Ligand Based on ab Initio Calculations," ***Organometallics*** 24, 1578 (2005)

List of Presentations

International Conferences

1. Hyo Jung Kim, Jeong-Hwan Lee, Ji Whan Kim, Sunghun Lee, Junhyuk Jang, Jang-Joo Kim, Hyun Hwi Lee, "Molecular alignment and nanostructure of 1,4,5,8,9,11-hexaazatriphenylene-hexanitrile (HATCN) thin films on organic surfaces," GPVC 2012, Nov. 19-21, 2012

2. Tae-Min Kim, Ji Whan Kim, Hyun Sub Shim, Jang-Joo Kim, "High efficiency and high photo-stability zinc-phthalocyanine based planar heterojunction solar cells with a double interfacial layer," ILCC 2012, Oct. 19~24, 2012

3. Tae-Min Kim, Ji Whan Kim, Hyun Sub Shim, Jang-Joo Kim, "High efficiency and high photo-stability zinc-phthalocyanine based planar heterojunction solar cells with a double interfacial layer," 2nd ENGE 2012, Sep. 17, 2012

4. Hyun-Sub Shim, Hyo Jung Kim, Ji Whan Kim, Sei-Yong Kim, Won-Ik Jeong, Tae-Min Kim and Jang-Joo Kim, "Enhancement of Near-Infrared absorption with high fill factor in lead phthalocyanine based organic solar cells," IMID2012, Aug. 28, 2012

5. Hyun-Sub Shim, Jang-Joo Kim, Hyo Jung Kim, Ji Whan Kim, Sei-Yong Kim, Won-Ik Jeong, Tae-Min Kim, "Enhanced sensitivity to near-infrared with high fill factor in small molecular organic solar cells," SPIE2012, Aug. 12 2012

6. Hyo Jung Kim, Ji Whan Kim, Hyun Hwi Lee, Byeondu Lee, Jang-Joo Kim, "GISAXS studies of initial growth mode and nanostructure of bulk heterojunction layers in planar type metal phthalocyanine molecules," SPIE2012, Aug. 12, 2012

7. Jeong-Hwan Lee, Ji Whan Kim, Sei-Yong Kim, Seung-Jun Yoo, Jae-Hyun Lee, Jang-Joo Kim, "An organic p-n junction for electrode-independent electron injection layer in organic light emitting diodes," SPIE 2012, Aug. 12, 2012

8. Jeong-Hwan Lee, Ji Whan Kim, Sei-Yong Kim, Seung-Jun Yoo, Jae-Hyun Lee, Jang-Joo Kim, "Electrode-independent Electron injection using an organic p-n junction for flexible organic light emitting diodes," MRS 2012, Apr. 13, 2012

9. Tae-Min Kim, Ji Whan Kim, Hyun-Sub Shim and Jang-Joo Kim, "High Efficiency and high photo-stability zinc-phthalocyanine based planar heterojunction solar cells with a double interfacial layer," MRS 2012, Apr. 12, 2012

10. Tae-Min Kim, Ji Whan Kim, Hyun Sub Shim and Jang-Joo Kim, "High efficiency and high photo-stability zinc-phthalocyanine based planar heterojunction solar cells with a double interfacial layer", The 3rd Asian Conference on Organic Electronics, Nov. 4-6 2011

11. Ji Whan Kim, Hyo Jung Kim, Tae-Min Kim, Tae Gun Kim, Jeong-Hwan Lee, Jeong Won Kim and Jang-Joo Kim, "Enhanced performance of organic planar heterojunction solar cell by controlling the molecular orientation", The 3rd Asian Conference on Organic Electronics, Nov. 4-6 2011

12. Ji Whan Kim, Hyo Jung Kim, Tae-Min Kim, Hyun Hwi Lee, Jang-Joo Kim, "Efficient small molecular bulk heterojunction solar cells using alternative thermal deposition", JSPS Asian Core Program Workshop/The 7th TU-SNU-UT Student Workshop, Oct. 19-22, 2011

13. Ji Whan Kim, Hyo Jung Kim, Tae-Min Kim, Hyun Hwi Lee, Jang-Joo Kim, "Small molecular bulk heterojunction solar cells using alternative thermal deposition", The 11th International Meeting on Information Display, Oct. 11-15, 2011

14. Hyo Jung Kim, Ji Whan Kim, Tae-Min Kim, Junhyuk Jang, Hyun Hwi Lee, "Controlling of initial molecular arrangement of copper(II) phthalocyanine for interpenetrating networks in a mixed

donor/acceptor layer", SPIE Optics+Photonics, Aug. 21-25, 2011

15. Hyo Jung Kim, Ji Whan Kim, Hyun Hwi Lee, Tae-Min Kim, Jang-Joo Kim, "Nano structures of the mixed layer in the small molecular organic photovoltaics", Nano Korea 2011 Symposium, Aug. 24-26, 2011

16. Ji Whan Kim, Hyo Jung Kim, Hyun Hwi Lee, Tae-Min Kim, and Jang-Joo Kim, "Formation of small molecular bulk heterojunctions by alternative thermal deposition", The 22nd International Conference on Molecular Electronics and Devices, May 19-20, 2011, Pohang (Korea)

17. Ji Whan Kim, Hyo Jung Kim, Hyun Hwi Lee, Tae-Min Kim, Jang-Joo Kim, "Alternative thermal deposition for high efficiency small molecular organic photovoltaics", The Asian Conference on Organic Electronics 2010 & The Asian Symposium on Organic Materials for Electronics and Photonics 2010, Nov. 3-5, 2010

18. Hyo Jung Kim, Ji Whan Kim, Hyun Hwi Lee, Tae-Min Kim, Jang-Joo Kim, "The application of x-ray scattering in nano structural studies in organic thin films", The Asian Conference on Organic Electronics 2010 & The Asian Symposium on Organic Materials for Electronics and Photonics 2010, Nov. 3-5, 2010

19. Ji Whan Kim, Hyo Jung Kim, Tae-Min Kim, Jane Lee, Jang-Joo Kim,

"Organic photovoltaics using controlled growth of small molecular bulk heterojunctions", SPIE Optics+Photonics, Aug. 1-5, 2010

20. Dong-Seok Leem, Paul H. Wöbkenberg, Sungsoo Kim, Jingsong Huang, Xuhua Wang, Ji Whan Kim, Jang-Joo Kim, Thomas D. Anthopoulos, John C. de Mello, Donal D. C.Bradley, "Interlayer Lithographic Patterning of Flexible Electrodes for Plastic Electronic Devices", Plastic Electronics EU 2009, Oct. 27-29, 2009

21. Hyung-Dol Park, Jae-Wook Kang, Deug-Sang Lee, Ji Whan Kim, Won-Ik Jeong, Young-Seo Park, Se-Hyung Lee, Kyungmoon Go, Jong-Soon Lee, Hyong-Jun Kim, and Jang-Joo Kim, "A Stable and Efficient Host Material Having Tetraphenylsilane for Phosphorescent Organic Light Emitting Diodes", IMID/IDMC/Asia Display 2008, Oct. 13-17, 2008

22. Junhyuk Jang, Ji Whan Kim, Nohhwal Park and Jang-Joo Kim, "Air stable n-type organic field effect transistors using a perfluoropolymer insulator", IMID/IDMC/Asia Display 2008, Oct. 13-17, 2008

23. Ji Whan Kim, Sei Yong Kim, and Jang-Joo Kim, "Amplified Spontaneous Emission in Hetero-structured Organic Semiconductors using very thin medium", The 19th International Conference on Molecular Electronics & Devices, May 29-30, 2008

24. Jae-Hyun Lee, Dong-Seok Leem, Ji Whan Kim, and Jang-Joo Kim, “High performance top-emission organic light emitting diodes with copper iodide doped hole injection layer”, 2008 MRS spring meeting, Mar. 24-28, 2008

25. Ji Whan Kim, Sei-Yong Kim, and Jang-Joo Kim, “Position sensitivity of amplified spontaneous emission with ultra thin organic gain medium”, 2008 MRS spring meeting, Mar. 24-28, 2008

26. Jae-Wook Kang, Ji-Whan Kim, Hyung-Dol Park, Deug-Sang Lee, Kyoungmoon Go, Jongsoon Lee, and Jang Joo Kim, “High Operational Stability of electrophosphorescent devices”, 2006 A recent advance in EL, display & lighting, Sep. 21, 2006

27. Joo Hyun Kim, Do Yeung Yoon, Ji Whan Kim and Jang Joo Kim, “New host materials with high triplet energy level for the electrophosphorescent device”, 2006 MRS spring meeting, Apr. 17-21, 2006

28. Ji Whan Kim, Joo Hyun Kim, Do Yeung Yoon and Jang Joo Kim, “Effect of Interfacial exciton blocking layer in blue emitting electrophosphorescent organic light emitting diodes”, 2006 MRS spring meeting, Apr. 17-21, 2006

29. Cheng-guo An, Jeong-Wook Oh, Hyung-Dol Park, Won-Ik Jeong, Ji

Whan Kim, Jae-Wook Kang, Ha-Suck Kim, Jang-Joo Kim, "Degradation mechanisms of green phosphorescent dye doped polymer light-emitting diodes", MRSociety spring meeting, April 17-21, 2006, San Francisco, CA, USA

30. Ji Whan Kim, Joo Hyun Kim, Do Yeung Yoon and Jang Joo Kim, "Improvement of electro-luminescent efficiency by using interfacial exciton blocking layer in blue emitting electrophosphorescent organic light emitting diodes", Jul. 19-23, 2005

Domestic conference

31. Ji Whan Kim, Tae-Min Kim, Hyun Hwi Lee, Jang-Joo Kim, Hyo Jung Kim "The role of CuI layer on the molecular arrangement of copper(II) phthalocyanine in a mixed donor/acceptor layer", 2011 Fall Meeting, the Polymer Society of Korea, Apr. 7-8, 2011

32. Ji Whan Kim, Sei-Yong Kim, Jang-Joo Kim, "Amplified spontaneous emission in an organic semiconductor with ultra thin gain medium", 2007 Fall Meeting, the Polymer Society of Korea, Oct. 11-12, 2007

33. Junhyuk Jang, Ji Whan Kim, Nohhwal Park and Jang-Joo Kim, "Stability of organic field effect transistors using a perfluoro polymer

insulator", 2007 Fall Meeting, the Polymer Society of Korea, Oct. 11-12, 2007

34. Dong-Seok Leem, Hyung-Dol Park, Jae-Wook Kang, Jae-Hyun Lee, Ji Whan Kim, Jang-Joo Kim, "Low-drive-voltage organic light-emitting diodes with rhenum oxide-doped hole transport layer", 2007 Spring Meeting, the Polymer Society of Korea, Apr. 12-13, 2007

35. Ji Whan Kim, Joo Hyun Kim, Do Yeung Yoon and Jang Joo Kim, "Improvement of electro-luminescent efficiency by using interfacial exciton blocking layer in blue emitting electrophosphorescent organic light emitting diodes", 2005 Fall Meeting, the Polymer Society of Korea, Oct. 13-14, 2005

Patents

1. Jang-Joo Kim, Ji Whan Kim, Hyo Jung Kim, “Method for formation of small molecule thin film and small molecule organic solar cell including bulk heterojunction”, PCT/KR2012/000953
2. Jang-Joo Kim, Tae-Min Kim, Ji Whan Kim, “Small molecular organic solar cells with a double interfacial layer,” Korean Patent, Application Nr. 10-2012-0055529
3. Jang-Joo Kim, Jeong-Hwan Lee, Ji Whan Kim, Sei-Yong Kim, “Inverted organic light-emitting diode and display apparatus including the same”, Korean Patent, Application Nr. 10-2012-0018060
4. Jang-Joo Kim, Ji Whan Kim, Hyo Jung Kim, “Method for formation of small molecule thin film and small molecule organic solar cell including bulk heterojunction”, Korea Patent, Application Nr. 10-2011-0011623
5. Jang-Joo Kim, Jeong-Hwan Lee, Ji Whan Kim, “Inverted organic light-emitting diode and flat display device comprising the same”, Korea Patent, Application Nr. 10-2010-0140556

Proceedings

1. Hyung-Dol Park, Jae-Wook Kang, Deug-Sang Lee, Ji Whan Kim, Won-Ik Jeong, Young-Seo Park, Se-Hyung Lee, Kyungmoon Go, Jong-Soon Lee, Hyong-Jun Kim, andJang-Joo Kim, “A Stable and Efficient Host Material Having Tetraphenylsilane for Phosphorescent Organic Light Emitting Diodes”, IMID/IDMC/Asia Display 2008, pp. 503-505, Oct. 13-17, 2008

2. Junhyuk Jang, Ji Whan Kim, Nohhwal Park and Jang-Joo Kim, “Air stable n-type organic field effect transistors using a perfluoropolymer insulator”, IMID/IDMC/Asia Display 2008, pp. 276-279, Oct. 13-17, 2008

3. Ji Whan Kim, Joo Hyun Kim, Do Yeung Yoon, Jang-Joo Kim, “Improvement of electroluminescent efficiency by using interfacial exciton blocking layer in blue emitting electrophosphorescent organic light emitting diodes”, Proceedings of International Meeting on Information Display 2, pp. 1381-1382, 2006